IOP Publishing Journal of Physics: Condensed Matter
J. Phys.: Condens. Matter **37** (2025) 033001 (21pp) https://doi.org/10.1088/1361-648X/ad882b

Topical Review

Recent advances in understanding and manipulating magnetic and electronic properties of EuM_2X_2 (M = Zn, Cd; X = P, As)

Xiyu Chen, Shuai Dong and Zhi-Cheng Wang*

Key Laboratory of Quantum Materials and Devices of Ministry of Education, School of Physics, Southeast University, Nanjing 211189, People's Republic of China

E-mail: wzc@seu.edu.cn

Received 25 July 2024, revised 2 September 2024
Accepted for publication 17 October 2024
Published 1 November 2024

Abstract

Over the past five years, significant progress has been made in understanding the magnetism and electronic properties of $CaAl_2Si_2$-type EuM_2X_2 (M = Zn, Cd; X = P, As) compounds. Prior theoretical work and experimental studies suggested that $EuCd_2As_2$ had the potential to host rich topological phases, particularly an ideal magnetic Weyl semimetal state when the spins are polarized along the c axis. However, this perspective is challenged by recent experiments utilizing samples featuring ultra-low carrier densities, as well as meticulous calculations employing various approaches. Nonetheless, the EuM_2X_2 family still exhibit numerous novel properties that remain to be satisfactorily explained, such as the giant nonlinear anomalous Hall effect and the colossal magnetoresistance effect. Moreover, EuM_2X_2 compounds can be transformed from semiconducting antiferromagnets to metallic ferromagnets by introducing a small number of carriers or applying external pressure, and a further increase in the ferromagnetic transition temperature can be achieved by reducing the unit cell volume. These features make the EuM_2X_2 family a fertile platform for studying the interplay between magnetism and charge transport, and an excellent candidate for applications in spintronics. This paper presents a comprehensive review of the magnetic and transport behaviors of EuM_2X_2 compounds with varying carrier densities, as well as the current insights into these characteristics. An outlook for future research opportunities is also provided.

Keywords: $CaAl_2Si_2$-type EuM_2X_2, carrier density, magnetism manipulation, tunable resistivity, magnetic semiconductor

1. Introduction

The trigonal $CaAl_2Si_2$-type EuM_2X_2 (M = Zn, Cd; X = P, As) were first synthesized decades ago [1, 2]. Reports on their crystal structures and basic magnetic and transport properties revealed them to be Zintl phases with a narrow bandgap and an antiferromagnetic (AFM) ground state [3, 4]. However, these Eu-based materials did not garner significant attention, save for the potential of antimonides in thermoelectric applications [5, 6]. This situation remained until the recent surge in research on magnetic topological materials. Among

* Author to whom any correspondence should be addressed.

the EuM_2X_2 compounds, $EuCd_2As_2$ first attracted substantial interest due to its structural similarity to the Dirac semimetal (DSM) Cd_3As_2 and complex interplay of magnetism and band topology [7, 8]. It exhibits an AFM transition at a Néel temperature (T_N) of 9.5 K, characterized by an A-type AFM structure [3, 8, 9]. Weyl semimetal state (WSM) or DSM state below T_N was claimed, based on the different angle-resolved photoemission spectroscopy (ARPES) results [10–12]. Furthermore, theoretical and experimental investigations suggest that $EuCd_2As_2$ is an ideal candidate for a magnetic WSM, featuring a *c*-axis polarized state [11, 13, 14]. And a Weyl state may potentially be induced by ferromagnetic (FM) spin fluctuations in the paramagnetic (PM) phase [10]. Due to its strong spin–orbit coupling (SOC), the band structure of $EuCd_2As_2$ is highly sensitive to spin canting [15]. This sensitivity leads to the observation of a pronounced nonlinear anomalous Hall effect (NLAHE), attributed to the spin-dependent band structure and its associated momentum-space Berry curvature [8, 16, 17]. Given the plethora of exotic phenomena it exhibits, $EuCd_2As_2$ stands out as the most intensively studied member of the EuM_2X_2 family [18–24]. However, the views about the nontrivial band topology of $EuCd_2As_2$ have been challenged by the recent experiments and theoretical calculations [25–28]. Earlier studies indicated that the temperature-dependent resistivity was predominantly metallic [8, 9]. Yet, recent investigations utilizing single crystals with reduced carrier densities ($n_h \approx 10^{15}$ cm^{-3}) suggest that $EuCd_2As_2$ is indeed a magnetic semiconductor rather than a WSM [25–27].

Inconsistent properties are also observed across other members of the EuM_2X_2 family. Wang *et al* reported that $EuZn_2As_2$ is an antiferromagnet with T_N of 19.6 K, displaying a bad-metal behavior with a carrier density of 8.6×10^{17} cm^{-3} at 200 K, and shows a negative magnetoresistance (nMR) of -300% [magnetoresistance defined as MR $= 100\% \times (\rho(H) - \rho(0))/\rho(H)$] near T_N [29]. Crystals of $EuZn_2As_2$ grown by Blawat *et al* showed a significantly higher carrier density, approximately 4×10^{20} cm^{-3}, yet exhibited a comparable nMR effect [30]. More recently, Luo *et al* succeeded in growing single crystals of $EuZn_2As_2$ with a notably lower carrier density ($n_h = 1.45 \times 10^{17}$ cm^{-3} at 200 K) revealing a semiconducting nature below 100 K, accompanied by a colossal magnetoresistance (CMR) effect. And a topological phase transition is believed to be induced by pressure [31]. Intriguingly, despite the variations in transport behavior, the reported T_N values for $EuZn_2As_2$ across these studies are nearly identical. The disparate transport properties can likely be attributed to differences in hole doping levels, associated with cation (Eu^{2+}) defects within the crystal lattice.

Regarding $EuZn_2P_2$ ($T_N = 23.5$ K), notable discrepancies in reported transport behaviors have been observed. Berry *et al* described $EuZn_2P_2$ as exhibiting insulating behavior, with resistivity reaching magnitudes far exceeding 10^4 Ω cm at 100 K [32]. Conversely, Krebber *et al* reported a resistivity of merely 0.06 Ω cm at the same temperature, alongside the observation of a CMR effect under magnetic field [33]. Moreover, $EuCd_2P_2$ ($T_N = 11$ K), the Cd analogue of $EuZn_2P_2$, stands out as a distinct member within the EuM_2X_2 family. Unlike its sibling compounds, $EuCd_2P_2$ shows a resistivity peak above T_N, attributed to pronounced magnetic fluctuations, whereas the peaks for other EuM_2X_2 compounds are situated precisely at T_N. Wang *et al* reported a resistivity peak at 18 K and a remarkably high CMR effect, exceeding $10^4\%$, upon suppression of the peak with a magnetic field [34]. By contrast, Zhang *et al* reported both the resistivity peak (at 14 K) and the CMR effect for $EuCd_2P_2$ to be several orders of magnitude larger [35].

Fundamentally, the diverse properties manifested by the same EuM_2X_2 compound can be ascribed to the intrinsic sensitivity of its narrow electronic bandgap to variations in carrier concentration, coupled with the spin configurations at the Eu sites. In the cases discussed, the synthesis protocols significantly impact the carrier density within the crystals, thereby influencing the ultimate properties of EuM_2X_2 materials. This variability presents opportunities to manipulate the properties of EuM_2X_2 compounds through adjusting the doping level by changing crystal growth conditions, employing chemical doping strategies, or utilizing other techniques such as hydrostatic pressure and electrostatic gating. In fact, recent studies on EuM_2X_2 ($M =$ Zn, Cd; $X =$ P, As) crystals grown using the molten salt flux method demonstrate that the application of this technique not only alters the electrical transport properties significantly, but also enables tuning of the magnetic orders from AFM to FM states [36–39]. This transformation is facilitated by the increased Eu defects introduced by the salt flux method, which is supported by the corresponding single crystal refinement data. The enhanced carrier concentration resulting from these defects induces interlayer FM interactions, leading to a FM ground state. Notably, this transition can be achieved with just a few percent of Eu vacancies or even less [38, 39].

Recent reports on the diverse physical properties underscore that the EuM_2X_2 family ($M =$ Zn, Cd; $X =$ P, As) exhibits highly tunable magnetism and charge transport, positioning it as a promising material system for future technological applications. Therefore, it is imperative to review the advances in comprehending and manipulating the magnetic and transport properties of EuM_2X_2 compounds. Firstly, we will succinctly outline the crystal structure, synthesis procedures, and the contradictory theoretical predictions surrounding EuM_2X_2. Following that, we will contrast the physical properties of heavily hole-doped versus low-carrier-density AFM-EuM_2X_2 crystals, encompassing magnetism, transport properties, pressure effects, and chemical doping. Subsequently, we will delve into the novel properties exhibited by FM-EuM_2X_2 samples obtained through the salt flux method. Finally, we will summarize a phase diagram delineating the relationship between resistivity magnitude and carrier density, which clearly elucidates the interplay between magnetism and charge transport. Given the vast body of research on the EuM_2X_2 family, attempting to provide comprehensive coverage is neither practical nor necessary; hence, this review selectively focuses on salient studies related to the property manipulation of EuM_2X_2 materials. For instance, the Eu-based antimonides will not be specifically highlighted, since of the relative scarcity of

research on property manipulation [40–42]. The overarching goal of this review is to present an overview of the varied properties of EuM_2X_2 compounds, identify the primary factors influencing their magnetism and transport behaviors, and outline the experimental strategies required to effectively manipulate the properties of the EuM_2X_2 family for advanced applications.

2. Crystal structure

EuM_2X_2 (M = Zn, Cd; X = P, As) crystallizes in a $CaAl_2Si_2$-type structure (trigonal, space group P-3m1, No. 164), as depicted in figure 1. The Eu^{2+} ions are arranged in a triangular lattice within the ab plane. M atoms occupy the centers of the MX_4 tetrahedra, and the tetrahedra form the quasi-two-dimensional $[M_2X_2]^{2-}$ frameworks through edge-sharing. The layers of Eu^{2+} ions are connected by the anionic $[M_2X_2]^{2-}$ slabs. Indeed, the $CaAl_2Si_2$-type structure is prevalent among ternary Zintl compounds containing rare-earth or alkaline-earth elements [43]. Concerning Eu-based compounds, over a dozen phases have been identified, exemplified by $EuAl_2Ge_2$, $EuMg_2Bi_2$ and $EuMn_2As_2$, with many exhibiting an A-type AFM ordering [44–46]. This review specifically addresses the Zn and Cd variants, whose crystallographic parameters listed in table 1.

3. Crystal growth methods

Single crystals of EuM_2X_2 can be grown using the metal flux or molten salt flux, both of which are detailed in this section. These differing growth techniques result in crystals with variable carrier densities. In fact, before the extensive investigations on $CaAl_2Si_2$-type EuM_2X_2 compounds, it was recognized that defects at the cation sites can significantly impact electronic properties, as evidenced by studies on AZn_2Sb_2 (A = Sr, Ca, Yb, Eu) as prospective thermoelectric materials [47–49]. The concentrations of A-site cation vacancies are strongly dependent on the cation electronegativity and sample growth conditions. The primary focus of this review will be on elucidating the vacancy-controlled magnetic and charge transport properties of EuM_2X_2. It is noteworthy to emphasize that, although the diverse crystal growth techniques yield samples with distinct transport properties, the crystal structure remains essentially unchanged. The main alteration discerned across these crystals manifest in the variation of carrier concentration.

Conventional metal flux method. The metal flux method is a common way to grow the crystals of EuM_2X_2, utilizing Sn (or Bi) as the flux [10, 50]. The density of intrinsically formed cation vacancies is contingent upon the purity of the initial materials and the specific crystal synthesis process. Despite variations, the procedures outlined in various publications are largely the same: the elements are mixed with Sn at a ratio EuM_2X_2:Sn = 10–30, then heated to a high temperature between 800 °C–1150 °C for an extended duration from several hours to 36 h. Following this, the mixture undergoes a gradual cool-down at a rate of 2 °C–3 °C per hour before the crystals are separated via centrifugation. However, the resultant hole concentrations and properties of EuM_2X_2 crystals, can exhibit considerable variability when produced through this method. As an illustrative case, $EuCd_2As_2$ has been reported to yield both insulating samples with $n \sim 10^{13}$ cm^{-3} and metallic samples with $n \sim 10^{19}$ cm^{-3} [10, 27]. Despite the diversity in charge transport characteristics observed across these samples, their ground states intriguingly converge on antiferromagnetism, marked by a consistent T_N.

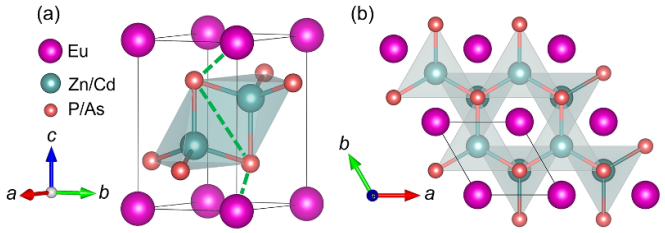

Figure 1. The crystal structure of EuM_2X_2 (M = Zn, Cd; X = P, As). Two distinct views of the crystal structure are presented in panels (a) and (b), respectively. The green dashed line shows the path for the interlayer superexchange interaction.

Modified Sn flux method. We notice that the recipes for the Sn flux method, as detailed in several publications, deviate subtly from the conventional procedure. Santos-Cottin *et al* adopted a two-step process to grow $EuCd_2As_2$ crystals, where the initial growth products served as seed material for the final growth, thereby increasing the crystal size and quality [25]. Through this approach, they obtained $EuCd_2As_2$ samples featuring a bandgap of about 770 meV. In another study about $EuZn_2P_2$, Krebber *et al* used a graphite crucible rather than the alumina crucible as the container for the starting materials, which yields samples with significantly lower resistivity compared to those reported elsewhere [33]. Although the specific impact of the graphite crucible was not explicitly elucidated, a plausible hypothesis is that the subtle replacement of phosphorus with carbon may underlie the enhanced electrical conductivity. Interestingly, Usachov *et al* synthesized crystals of $EuCd_2P_2$ using the graphite crucible [51], revealing a complex magnetic behavior and a more pronounced CMR effect compared to the sample in [34].

Salt flux method. In the early stages, Schellenberg *et al* synthesized $EuCd_2As_2$ single crystals using the salt flux method, with a molar ratio of $EuCd_2As_2$ to an equimolar mixture of NaCl/KCl set at 1:4, which yielded crystals displaying an AFM ground state [3]. Later, Jo *et al* achieved the first successful growth of $EuCd_2As_2$ crystals with a FM state using the same salt flux method, albeit with a mass ratio of $EuCd_2As_2$ to the salt mixture adjusted to 1:4, translating to a molar ratio of 1:16 [36]. This suggests that the FM sample was grown in a more dilute solution. Furthermore, Jo *et al* also synthesized AFM-$EuCd_2As_2$ crystals in the dilute salt flux environment by increasing the proportion of Eu, setting the ratio to Eu:Cd:As = 1.75:2:2 [36]. Both the use of a concentrated flux and the heightened proportion of Eu indicate that AFM-$EuCd_2As_2$ crystals should possess fewer Eu vacancies than

Table 1. The cell parameters, Néel temperatures (T_N), and Weiss temperatures (Θ_w) of AFM-EuM_2X_2 (M = Zn, Cd; X = P, As).

Compound	$a = b$ (Å)	c (Å)	c/a	V_{cell} (Å^3)	Eu T_N (K)	Θ_w	References
$EuZn_2P_2$	4.08497(18)	7.0019(4)	1.714	101.187(11)	23.5	19.2	[32]
$EuZn_2As_2$	4.211 18(3)	7.18114(6)	1.705	110.2888(24)	19.6	20.2	[29]
$EuCd_2P_2$	4.3248(2)	7.1771(7)	1.660	116.26	11.3	28.1	[34]
$EuCd_2As_2$	4.44016(4)	7.32779(9)	1.650	125.1125(38)	9.2	12.1	[29]

their FM counterparts, which is supported by crystal structural refinements. Very recently, our team successfully synthesized $EuCd_2P_2$, $EuZn_2As_2$, and $EuZn_2P_2$ crystals with FM ground states through the salt flux method [38, 39]. This achievement underscores the versatility of the salt flux method as a general strategy for modulating the ground state of $CaAl_2Si_2$-type EuM_2X_2 compounds.

4. Electronic structure

$EuCd_2As_2$ was initially deemed a promising candidate for hosting rich topological phases, which was supported by a plethora of experimental and theoretical investigations [8, 10–14]. However, recent studies on high-quality $EuCd_2As_2$ crystals, characterized by reduced carrier densities, have revealed $EuCd_2As_2$ is actually a magnetic semiconductor rather than the anticipated topological WSM [25–27]. Moreover, recent calculations by Cuono *et al* have underscored the significant influence of electron correlation effects on the electronic and topological properties of $EuCd_2As_2$ [28]. Previous theoretical studies, employing modest Hubbard U values (∼3–5 eV) within the standard generalized gradient approximation (GGA) functional, typically concluded that $EuCd_2As_2$ exhibits nontrivial topology. In contrast, computations utilizing the Heyd–Scuseria–Ernzerhof (HSE) hybrid functional + U and the strongly constrained and appropriately normed (SCAN) functional + U approaches tend to yield positive values of the energy gap, indicating a trivial band topology for $EuCd_2As_2$, which aligns more closely with experimental findings [25]. Shi *et al* further confirmed the underestimation of the Hubbard U in earlier studies by employing the linear response ansatz, determining a converged U value of approximately 8 eV [26]. In this section, we will first briefly summarize the statements from prior research that claimed the topologically nontrivial nature of $EuCd_2As_2$, followed by an exposition of the revised conclusions from Cuono *et al* [28] and associated insights into the electronic structure of EuM_2X_2 compounds.

Hua *et al* predicted $EuCd_2As_2$ would host a DSM state when the ground state assumes an A-type AFM structure with Eu spin aligned along the c axis (AFM$_c$) [14]. However, when the AFM structure features an in-plane spin configuration (AFM$_a$), the threefold rotation symmetry C_3 is broken, transforming $EuCd_2As_2$ to an AFM topological insulator. In a concurrent experimental study, Rahn *et al* revealed that the actual magnetic ground state of $EuCd_2As_2$ is AFM with spins lying in the ab plane [8]. Subsequently, Soh *et al* predicted the existence of a WSM phase, characterized by a single pair of Weyl nodes near the Fermi level, under the condition that Eu spins are fully polarized along the c axis [11]. This prediction was supported by their quantum oscillation and ARPES results. Wang *et al* reported a similar conclusion and further predicted that substituting half of the Eu sites with Ba could stabilize FM order [13]. The experimental results obtained by Ma *et al* showed quasi-static and quasi-long-range FM fluctuations in the PM phase of $EuCd_2As_2$, which could lead to band splitting and induce a WSM state [10]. The following year, Ma *et al* also claimed that a magnetic DSM-like band structure was observed via ARPES in the AFM state of $EuCd_2As_2$ [12].

These investigations appear robust enough to substantiate the nontrivial band topology of $EuCd_2As_2$. However, an optical spectroscopy study conducted by Santos-Cottin *et al*, utilizing low-carrier-density $EuCd_2As_2$, indicates that it is in fact a magnetic semiconductor with an optical gap of 0.77 eV [25]. Furthermore, the semiconducting $EuCd_2As_2$ sample grown by Shi *et al* exhibits a similar optical gap of 0.74 eV and a transport gap of 55.8 meV [26]. Electrical transport results of semiconducting $EuCd_2As_2$ will be presented in section 5.2. Directly following Santos-Cottin *et al*'s work, Cuono *et al* calculated the electronic properties of $EuCd_2X_2$ (X = P, As, Sb, Bi) using the HSE + U, SCAN + U, and GGA + U approaches [28]. Within GGA + U, they found that the sign of the band gap is highly sensitive to variations in the value of U, as illustrated in figure 2(a) [28]. For the AFM$_a$ ground state, a transition occurs from the topological to the trivial phase at U = 6.0 eV. When U = 7 eV with AFM$_a$ spin configuration, $EuCd_2As_2$ is in a trivial phase, featuring a notably narrow band gap of 40 meV [28]. The corresponding band structure is displayed in panel (b). Cuono *et al* compared the resulting E_g value from the GGA + U to those derived from HSE + U and SCAN + U in panel (c). They found that the latter two approaches yield much larger E_g values, and HSE + U provides a gap value of 0.79 eV that is highly consistent with experimental data [25, 26, 28]. Generally, GGA + U approach tends to underestimate the band gap due to its limitations, while computations utilizing hybrid functionals produce more accurate band gaps. Therefore, the excellent consistency of the gap values obtained from optical measurements and computation within HSE + U clearly indicates the semiconducting nature of $EuCd_2As_2$. An additional key insight from their computations is that the FM$_c$ phase exhibits a smaller gap than the AFM phases across all U values. Consequently, applying a magnetic field along the c axis invariably diminishes the band gap, which resonates with experimental observations in EuM_2X_2 materials and partially elucidates their nMR effect.

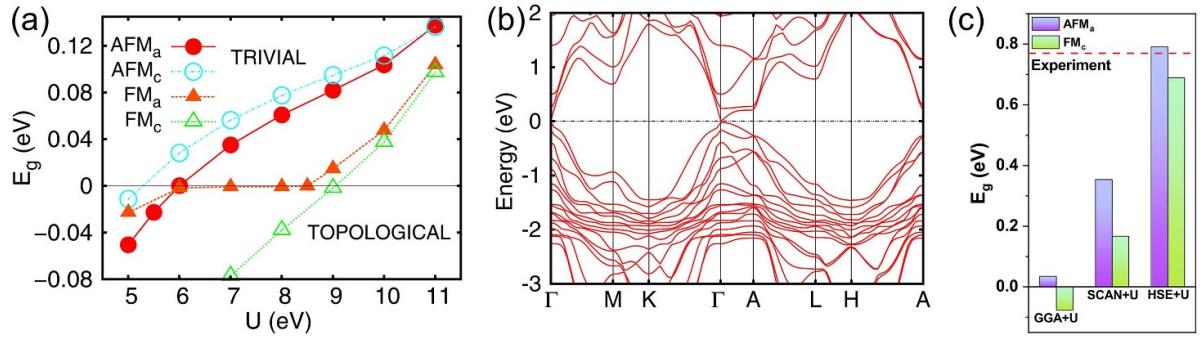

Figure 2. (a) Energy gap (E_g) for $EuCd_2As_2$ as a function of the Coulomb repulsion energy U. AFM$_a$: AFM phase with spins in the *ab* plane; AFM$_c$: AFM phase with spins along the *c* axis; FM$_a$: FM phase with spins in the *ab* plane; FM$_c$: FM phase with spins along the *c* axis. The negative values of E_g indicate a topological phase, whereas positive values represent a trivial phase. (b) Band structure $EuCd_2As_2$ in the A-type AFM configuration of by using GGA + U with $U = 7$ eV on the f orbitals of Eu. (c) E_g obtained within GGA + U, SCAN + U, HSE + U ($U = 7$ eV) for the AFM$_a$ and FM$_c$ phases. Reprinted figure with permission from [28], Copyright (2023) by the American Physical Society.

The trivial band gap of $EuCd_2P_2$, as computed by Cuono *et al*, is approximately 1.4 eV [28]. While the E_g values reported by Zhang *et al* and Chen *et al* are 819 meV and 380 meV, respectively, due to their use of different functionals and smaller Hubbard U values [35, 39]. Chen *et al* also compared the total energies of $EuCd_2P_2$ with and without Eu vacancies, under both AFM and FM spin configurations. Their analysis revealed that the interlayer FM coupling is more favored in the presence of Eu vacancies, which is consistent with the experimental observations [39]. Moreover, both $EuZn_2As_2$ and $EuZn_2P_2$, when in the AFM$_a$ state, are calculated to be trivial narrow-gap magnetic semiconductors [29, 31–33, 52].

5. Physical properties of AFM-EuM_2X_2

5.1. Magnetic properties

As previously mentioned, the magnetism in EuM_2X_2 compounds originates from the triangular lattice of Eu^{2+} ions with a $4f^7$ electronic configuration. All members of EuM_2X_2 (M = Zn, Cd; X = P, As) exhibit an A-type AFM order, implying that the Eu^{2+} spins couple ferromagnetically within the *ab* plane, whereas the interlayer interaction between Eu layers is AFM. Magnetic data for EuM_2X_2 are summarized in figure 3. Considering the similarity of the magnetic behavior, we use the data from $EuCd_2As_2$, shown in panels (a) and (b), as a representative example [9, 29]. Panel (a) reveals a transition peak at 9.2 K for both in-plane and out-of-plane magnetic susceptibility curves, indicating the emergence of AFM order in $EuCd_2As_2$. A notable disparity in susceptibility with the magnetic fields in different directions underscores the pronounced magnetocrystalline anisotropy in $EuCd_2As_2$, with the *ab* plane serving as the easy magnetization plane. A positive Weiss temperature ($\Theta_w = 12.1$ K) is derived from fitting the Curie-Weiss law $\chi_{ab} = \chi_0 + C/(T - \Theta_w)$ to the susceptibility data above 100 K, suggesting dominant FM interactions. Panel (b) shows the magnetization of $EuCd_2As_2$ for different field directions. Saturation fields for in-plane and out-of-plane directions are determined to be 0.8 T and 1.6 T, respectively, confirming the easy-plane anisotropy. The saturated moment (7.5 μ_B) under high fields and the effective moment of (8.3 μ_B) obtained from the Curie–Weiss fit corroborate the Eu^{2+} oxidation state.

$EuCd_2P_2$, $EuZn_2As_2$, and $EuZn_2P_2$ exhibit similar magnetic characteristics akin to those of $EuCd_2As_2$, with respective A-type AFM ordering temperatures of 11.3 K, 19.6 K, and 23.5 K, as shown in panels (c), (e), and (g) [29, 34]. The shared features across these compounds include: (1) the A-type AFM order, substantiated through neutron diffraction or resonant elastic x-ray scattering [8, 29, 33, 53, 54]; (2) the same easy magnetization plane (the *ab* plane); (3) the positive Weiss temperatures, as listed in table 1. Despite these commonalities, the differences in magnetocrystalline anisotropy are noticeable. $EuCd_2P_2$ shows a more pronounced anisotropy relative to $EuCd_2As_2$, evidenced by greater disparities in anisotropic susceptibilities and the conspicuous absence of an AFM peak in the in-plane susceptibility curve. This enhanced magnetic anisotropy stems from the reduced spatial extension of the *p* orbitals from As to P, leading to weakened interlayer coupling between Eu layers [34]. The weakened interlayer coupling further results in the intensified magnetic fluctuations and a resistivity peak above T_N, as shown in figure 6(a). In contrast, $EuZn_2As_2$ and $EuZn_2P_2$ display milder magnetic anisotropy, attributable to the more localized *d* orbitals and diminished SOC in the Zn compounds [29, 32, 52]. In the EuM_2X_2 family, FM fluctuations above T_N are commonly observed, playing a crucial role in facilitating certain exotic phenomena, such as the NLAHE [16, 55].

The ordering temperature of the Eu lattice depends on the specific M_2X_2 framework. Berry *et al* claimed that the magnetic interactions originate from the dipolar interactions, and that T_N values can be scaled through a linear combination of $1/d_{nn}{}^3$ (d_{nn} = intralayer Eu–Eu distance) and $1/d_{il}{}^3$ (d_{il} = interlayer Eu–Eu distance), with the coefficients close to a 1:−4 ratio [32]. However, Singh *et al* explained the

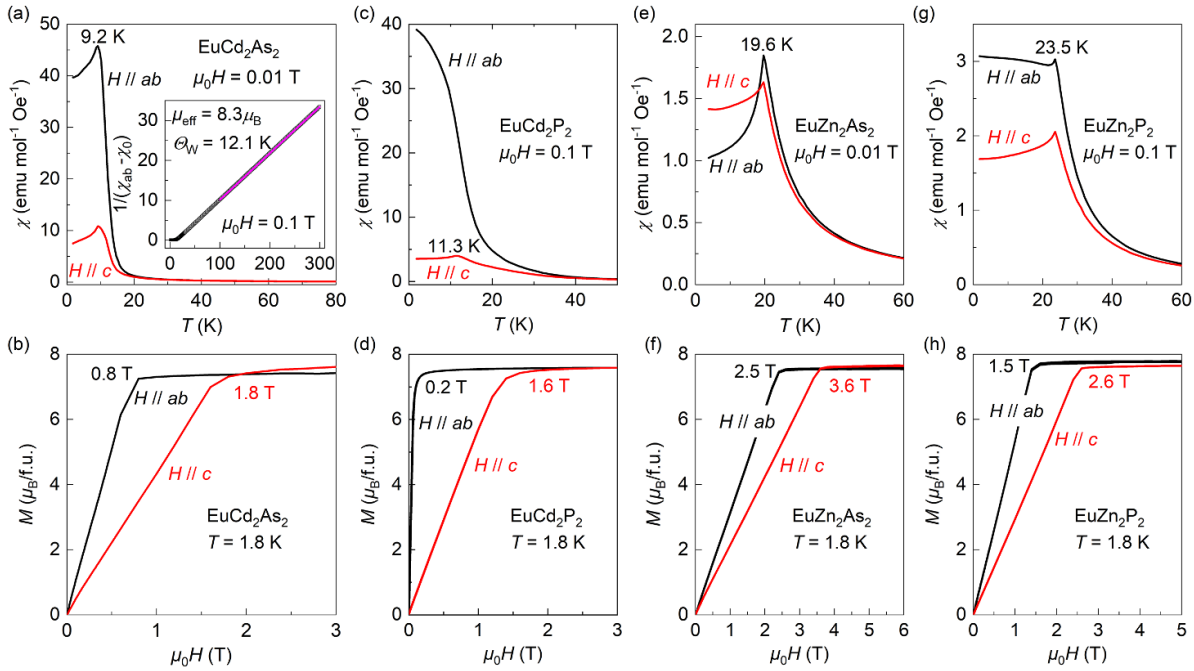

Figure 3. Temperature-dependent magnetic susceptibility of antiferromagnetically ordered $EuCd_2As_2$ (a), $EuCd_2P_2$ (c), $EuZn_2As_2$ (e), and $EuZn_2P_2$ (g) under both in-plane and out-of-plane fields. The inset of panel (a) displays the Curie–Weiss fit of $EuCd_2As_2$. Correspondingly, the in-plane and out-of-plane magnetization data at 1.8 K for each compound are illustrated in panels (b), (d), (f), and (h), respectively. Panels ((a), (b), (e), (f)) Reprinted figure with permission from [29], Copyright (2022) by the American Physical Society. Panels [(c), (d)] [34]. John Wiley & Sons. © 2021 Wiley-VCH GmbH.

magnetic interactions with an extended superexchange mechanism, which was supported by their simulation results using Monte Carlo method [52]. Based on the scheme proposed by Singh *et al*, the interlayer AFM coupling between two Eu sites along the *c* axis is mediated by two intervening pnictogen atoms, as illustrated by the green dashed line in figure 1(a). This superexchange mechanism effectively elucidates the variation in T_N across EuM_2X_2 compounds, taking into account the length of the Eu–*X*–*X*–Eu path. Among the quartet, $EuCd_2As_2$, featuring the longest Eu–As–As–Eu path (∼10.81 Å), consequently exhibits the lowest T_N. Conversely, $EuZn_2P_2$, with the shortest path (∼10.12 Å), presents the highest T_N.

Moreover, it appears that the T_N values and other magnetic properties of EuM_2X_2 do not fluctuate significantly with changes in carrier density of the crystals, provided that the ground state is AFM. This observation is substantiated by the consistent results from various independent studies. As shown in figure 4, comparisons of susceptibility and magnetization between the insulating and metallic phases of $EuCd_2As_2$ reveal negligible discrepancies [25]. The underlying rationale for this phenomenon could be that the AFM interactions, specifically the superexchange correlations in EuM_2X_2, predominantly hinge on the crystal structure. And a minor fraction of vacancies does not substantially modify the structure. However, when the FM interactions, triggered by the heavily doped carriers, become predominant, the ground state of EuM_2X_2 undergoes a sudden switch, which will be discussed further in section 6.2.2.

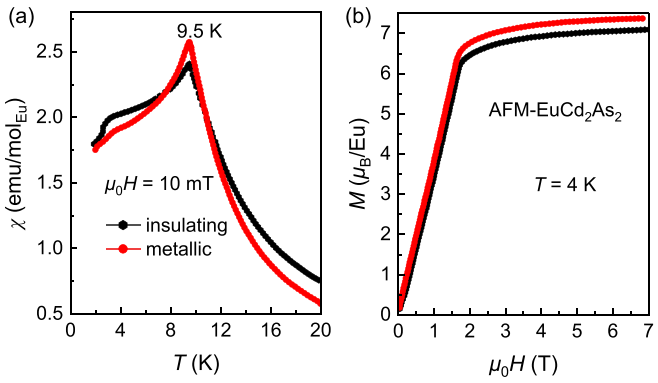

Figure 4. Comparisons of the $\chi(T)$ and $M(H)$ curves between metallic and insulating $EuCd_2As_2$. Reprinted figure with permission from [25], Copyright (2023) by the American Physical Society.

5.2. *Electrical transport properties*

In contrast to the relatively uniform magnetic properties, the electrical transport behaviors of compounds within the EuM_2X_2 family exhibit a far greater diversity and are acutely sensitive to variations in carrier concentration. In this section, we delve into comparisons between the same AFM-EuM_2X_2 materials with differing carrier concentrations. And we will sequentially introduce the charge transport properties of AFM-$EuCd_2As_2$, AFM-$EuCd_2P_2$, AFM-$EuZn_2As_2$, and AFM-$EuZn_2P_2$.

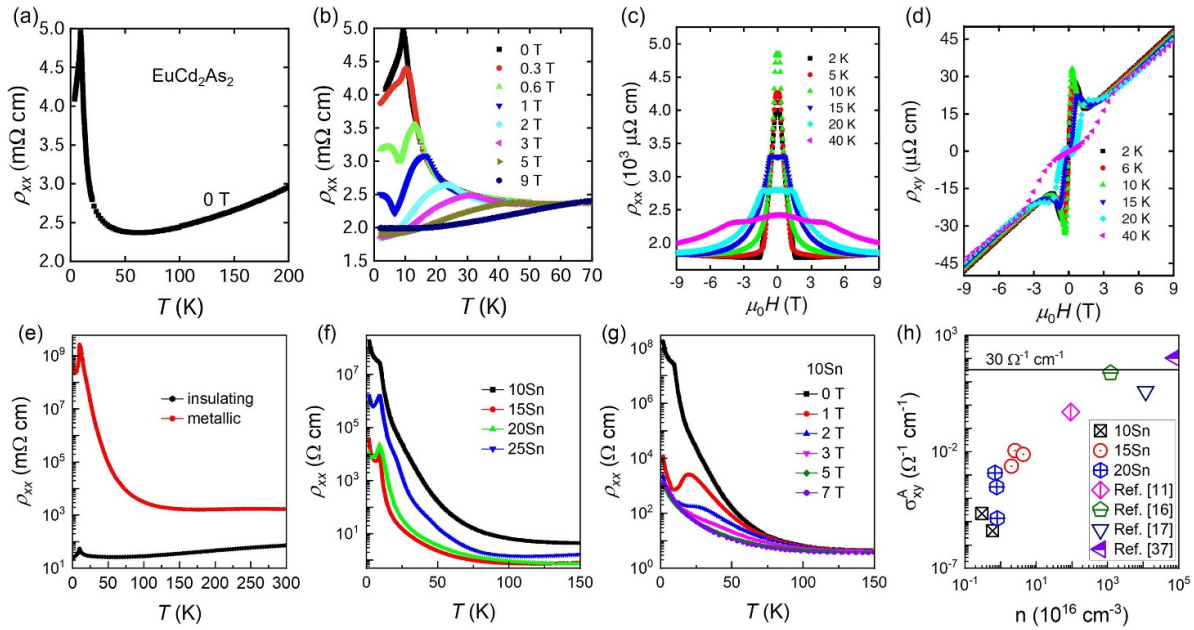

Figure 5. Electrical transport results of AFM-$EuCd_2As_2$ with metallic (a)–(d) and insulating (f)–(h) behaviors. (a) Temperature-dependent resistivity, $\rho_{xx}(T)$, of metallic $EuCd_2As_2$ under zero field. (b) $\rho_{xx}(T)$ under different fields. (c) The field-dependent ρ_{xx} measured at various temperatures. (d) Hall resistivity ρ_{xy} of metallic $EuCd_2As_2$. Reprinted figure with permission from [17], Copyright (2021) by the American Physical Society. (e) Comparison between $\rho_{xx}(T)$ of metallic and insulating $EuCd_2As_2$. Reprinted figure with permission from [25], Copyright (2023) by the American Physical Society. (f) $\rho_{xx}(T)$ of samples grown with the different ratios of Sn flux. (g) $\rho_{xx}(T)$ under different fields from the sample grown with 10 Sn. (h) Anomalous Hall conductivity $\sigma_{xy}{}^{A}$ versus carrier density n of samples from different sources [11, 16, 17, 26, 37]. Reprinted figure with permission from [26], Copyright (2024) by the American Physical Society.

5.2.1. Resistivity of AFM-$EuCd_2As_2$. Figures 5(a)–(d) shows the electrical transport properties of $EuCd_2As_2$ reported by Xu *et al* [17]. The longitudinal resistivity, ρ_{xx}, decreases as temperature goes down, and this metallic behavior persists above 50 K. Below 50 K, enhanced magnetic scattering triggers an increase in ρ_{xx}, peaking at T_N around 9.5 K, before declining again due to reduced scattering from the ordered Eu moments, as shown in figure 3(a). The resistivity peak at 9.5 K is notably diminished under the application of external magnetic fields. Figure 5(c) illustrates the ρ_{xx} versus H dependence at various temperatures. At 2 K, a nMR of approximately -300% is attained at $\mu_0 H \sim 1.5$ T with the definition that MR $= 100\% \times [\rho_{xx}(H) - \rho_{xx}(0)]/\rho_{xx}(H)$. ρ_{xx} reaches a minimum at 1.5 T, aligning with the saturation field of out-of-plane magnetization. Above T_N, a slight increase in ρ_{xx}(H) is observed in the low-field region, which may be attributed to the field-induced canting of the Eu spin towards the c axis.

The Hall resistivity, ρ_{xy}, of $EuCd_2As_2$ is shown in figure 5(d). The total Hall resistivity can be decomposed as $\rho_{xy} = R_0\mu_0 H + S_H{\rho_{xx}}^2 M + {\rho_{xy}}^{NL}$. The first term, $R_0\mu_0 H$, represents the ordinary Hall effect (OHE), where R_0 denotes a constant. The conventional anomalous Hall effect (AHE) is represented by the second term, $S_H{\rho_{xx}}^2 M$, with S_H being another constant. The final component, ${\rho_{xy}}^{NL}$, signifies the unconventional contribution to the AHE, i.e., NLAHE. As shown in figure 5(d), it is evident that ρ_{xy} varies markedly above and below T_N, which is influenced by differing contributions from ${\rho_{xy}}^{NL}$. Xu *et al* attributed this variation to the coexistence of two mechanisms below T_N: the real-space Berry phase driven topological Hall effect (THE) and the momentum-space Berry curvature associated with Weyl points. In contrast, only the latter mechanism contributes to ${\rho_{xy}}^{NL}$ above T_N [17]. Cao *et al* also reported a similar giant NLAHE in $EuCd_2As_2$, and explored its physical origin [16]. However, they claimed that the NLAHE in $EuCd_2As_2$ does not stem from the real-space THE or Weyl physics, but rather arises from the evolution of the band structure induced by spin rotation [16]. This explanation is grounded in the extreme sensitivity of the electronic structure to spin canting.

Recently, Santos-Cottin *et al* obtained ultraclean $EuCd_2As_2$ crystals through a two-step growth process [25]. These crystals exhibit insulating transport characteristics, yet their magnetic properties are virtually indistinguishable from those of metallic $EuCd_2As_2$ samples, as illustrated in figure 4. Figure 5(e) compares the resistivity of the insulating phase to that of the metallic phase, revealing discrepancies exceeding seven orders of magnitude at low temperatures. Based on experimental evidence from electronic transport, optical spectroscopy, and excited-state photoemission spectroscopy, Santos-Cottin *et al* proposed that the ultraclean $EuCd_2As_2$ is actually a magnetic semiconductor with a gap of about 770 meV, rather than a field-induced topological semimetal. Their results also indicate that the band gap of $EuCd_2As_2$ can be notably reduced in the magnetic field [25].

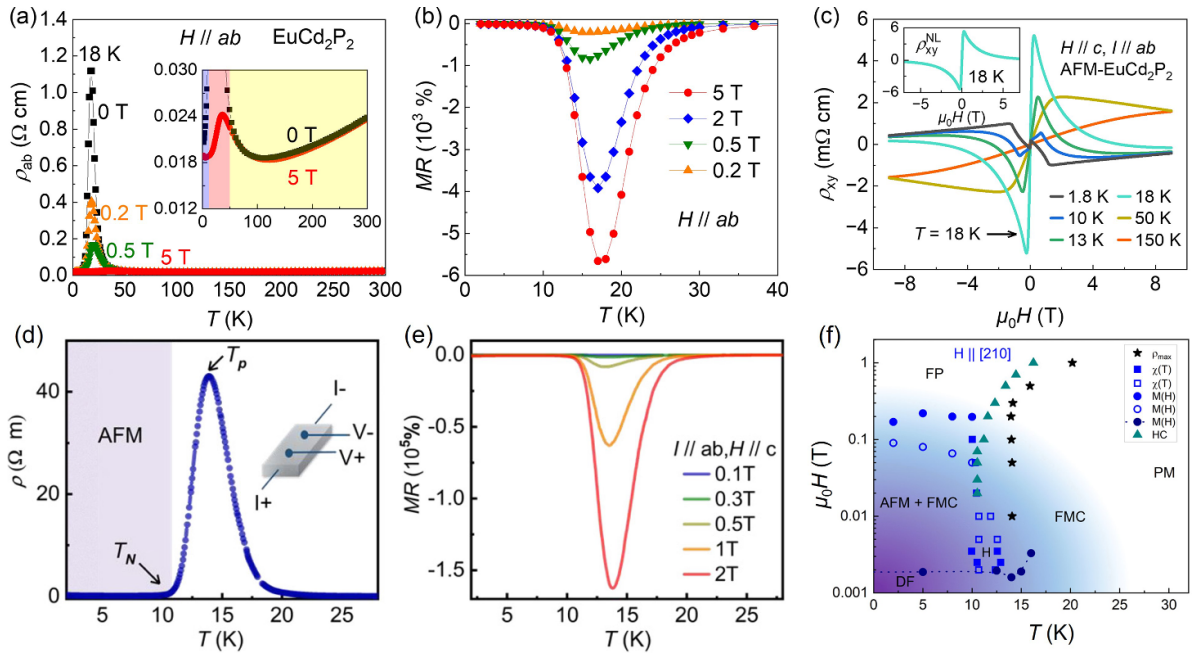

Figure 6. (a) Temperature-dependent resistivity of AFM-$EuCd_2P_2$ under various fields. Inset zooms in on the resistivity under 5 T. [34] John Wiley & Sons. © 2021 Wiley-VCH GmbH. (b) Temperature dependence of MR. [34] John Wiley & Sons. © 2021 Wiley-VCH GmbH. (c) Hall resistivity of AFM-$EuCd_2P_2$ as a function of field at different temperatures. Inset shows the NLAHE at 18 K. Reprinted figure with permission from [39], Copyright (2024) by the American Physical Society. ((d), (e)) Temperature-dependent resistivity and MR of AFM-$EuCd_2P_2$ with a lower carrier density. Reprinted figure with permission from [35], Copyright (2023) by the American Physical Society. (f) *H*–*T* phase diagram of AFM-$EuCd_2P_2$ for *H* // [210]. DF: domain flip; FP: field-polarized; PM: paramagnetic; FMC: FM clusters. Reprinted figure with permission from [51], Copyright (2024) by the American Physical Society.

Subsequently, several investigations have further confirmed the semiconductor nature of $EuCd_2As_2$. Shi *et al* synthesized a series of semiconducting $EuCd_2As_2$ samples by adjusting the ratio of Sn flux, yielding carrier concentrations ranging from 10^{15} to 10^{16} cm^{-3} in the crystals [26]. The resistivity curves from these samples are presented in figures 5(f) and (g). Similar to the metallic phase, the CMR effect is also observed in the semiconducting phase, with a significantly higher magnitude, as shown in figure 5(g). Through calculating the anomalous Hall conductivities (AHCs) in low-carrier-density $EuCd_2As_2$ and juxtaposing these against the metallic samples, Shi *et al* discovered a strong correlation between the AHC of $EuCd_2As_2$ and the carrier density, as illustrated in figure 5(h). This finding contrasts with the anticipated constant AHC derived from the Berry curvature associated with the separation of the Weyl nodes [56]. Moreover, Shi *et al* attributed the prior misidentification of the topological phase in $EuCd_2As_2$, as claimed in numerous theoretical studies, to an underestimation of the Hubbard *U* parameter [26].

In addition, Wang *et al* also carried out magneto-transport measurements on low-carrier-density (10^{13} cm^{-3}) $EuCd_2As_2$ crystals [27]. They found that the surface conduction dominates the transport due to band bending, which is diminished upon mechanical polishing of the crystal surfaces. Moreover, the resistance can be dramatically modulated by applying a *dc* bias current due to Fermi surface displacement in electric fields. This investigation further challenges the validity of the topological semimetal hypothesis about $EuCd_2As_2$.

5.2.2. Resistivity of AFM-$EuCd_2P_2$. Among the EuM_2X_2 compounds, $EuCd_2P_2$ was the first member to come to attention for exhibiting the CMR effect. Wang *et al* and Chen *et al* measured the in-plane resistivity and Hall effect of AFM-$EuCd_2P_2$ crystals, respectively [34, 39]. The samples are sourced from the same batch, and the results are summarized in figures 6(a)–(c), whose carrier density in these crystals is estimated to be $\sim 3.6 \times 10^{18}$ cm^{-3} at 200 K [39]. A pronounced resistivity peak is observed at 18 K under zero field, well above the T_N (11.3 K) for AFM-$EuCd_2P_2$. The peak is dramatically suppressed by a small field, leading to a giant CMR, as illustrated in figure 6(a). Three distinct temperature ranges are identified and highlighted in the inset: a yellow-shaded poor metallic region, a red-shaded intermediate CMR region, and a blue-shaded magnetic ordered region below T_N. The CMR maximum is situated at the temperature of the resistivity peak (T_{peak}), specifically within the red-shaded area, setting it apart from other EuM_2X_2 compounds where the temperature of the maximum nMR coincides with T_N. The calculated MR exceeds -10^3% in fields less than 1 T, as shown in figure 6(b) plotted against temperature. Wang *et al* ascribe the CMR of $EuCd_2P_2$ to strong FM fluctuations above T_N. Moreover, the Hall response of $EuCd_2P_2$ near the resistivity peak temperature is entirely dominated by the NLAHE by AFM-$EuCd_2P_2$, as demonstrated in figure 6(c). A similar decomposition analysis of the Hall resistivity, akin to that performed for $EuCd_2As_2$ (figure 5), was conducted. This analysis revealed that the contribution of the NLAHE can reach up to 97% at 0.25 T for the curve at 18 K [39]. Given the

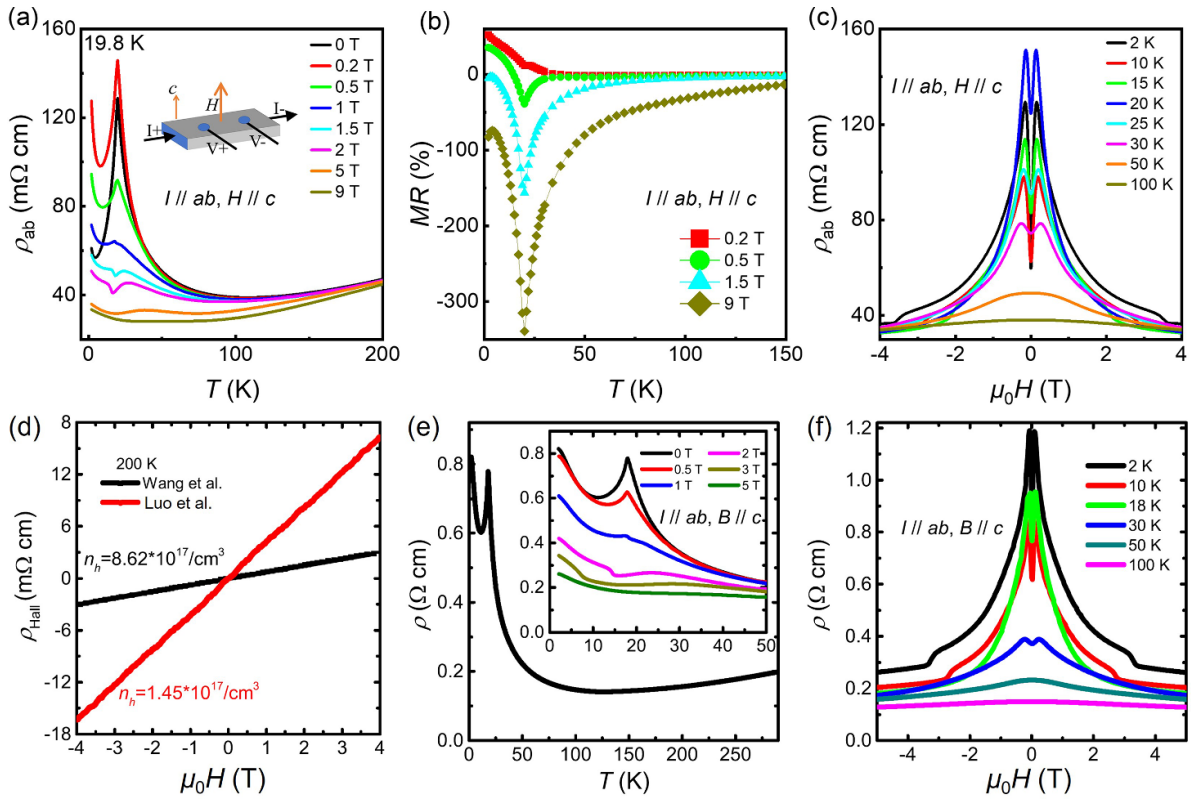

Figure 7. Electrical transport data of AFM-$EuZn_2As_2$ crystals with different carrier concentrations. Panels (a)–(c) shows the data from the sample with the higher carrier density. Reprinted figure with permission from [29], Copyright (2022) by the American Physical Society. Panels (d)–(f) show the results of the sample with the lower carrier density. Reprinted figure with permission from [31], Copyright (2023) by the American Physical Society. [(a), (e)] Temperature dependence of in-plane resistivity with fields along the *c* axis. (b) Temperature dependence of MR under different fields. [(c), (f)] Field dependence of the resistivity at several temperatures. (d) A comparison between the Hall effects from the two samples at 200 K.

topologically trivial band structure of $EuCd_2P_2$, the NLAHE may originate from a nonzero spin chirality related to the FM domains above T_N [54] or the evolution of the electronic structure induced by the external magnetic field [16]. Further experimental clarifications are needed to explain the NLAHE in $EuCd_2P_2$.

The origin of CMR in $EuCd_2P_2$ has attracted considerable research interest, as it clearly cannot be attributed to mechanisms analogous to those in manganites, given the absence of mixed valence or significant lattice distortion. Flebus *et al* posited a magnetic Berezinskii–Kosterlitz–Thouless transition as the explanation for the pronounced CMR [57, 58]. Furthermore, Homes *et al* and Sunko *et al* reported the emergence of FM clusters above the T_N, leading to carrier localization and an increase in resistivity via spin–carrier interactions [54, 59]. Zhang *et al* carried out ARPES to investigate the origin of CMR [35]. Their findings suggested an electronic structure reconstruction, transitioning from PM (above T_{peak}) to FM (between T_{peak} and T_N), and finally to AFM (below T_N). It is worth noting that the $EuCd_2P_2$ sample analyzed by Zhang *et al* exhibits characteristics distinct from those studied by Wang *et al*, as manifested by a resistivity peak and CMR effect approximately ten times greater, as illustrated in figures 6(d) and (e), along with a lower T_{peak} (14 K), indicative of a reduced carrier concentration in the crystal [34, 35]. In a recent study, Usachov *et al* examined the $EuCd_2P_2$ crystals synthesized using a graphite crucible [51]. Their electrical transport measurements also revealed a resistivity peak at 14 K rather than 18 K, yet the peak magnitude and CMR effect were comparable to the outcomes reported by Wang *et al* [34]. Contrary to Zhang *et al*'s observations [35], Usachov *et al*'s spectroscopic data showed no evidence of exchange splitting or substantial changes in the electronic structure [51]. Additionally, they constructed a *H*–*T* phase diagram of $EuCd_2P_2$ using magnetization, heat capacity, and transport data, as depicted in figure 6(f). Further experimentation is warranted to reconcile the discrepancies between different reports and elucidate the mechanisms underlying CMR phenomena above T_N in $EuCd_2P_2$.

5.2.3. Resistivity of AFM-$EuZn_2As_2$. Several teams have investigated the charge transport properties of AFM-$EuZn_2As_2$, yielding largely consistent results except for the carrier densities within the crystals and the absolute values of resistivity [29–31, 55]. $EuZn_2As_2$ was predicted to be a narrow-gap semiconductor by first-principles calculations [29]. However, it displays a bad-metal behavior at high temperatures (>100 K), as evidenced by the results from Wang *et al* (figures 7(a)–(c)) and Luo *et al* (figures 7(d)–(f)) [29, 31].

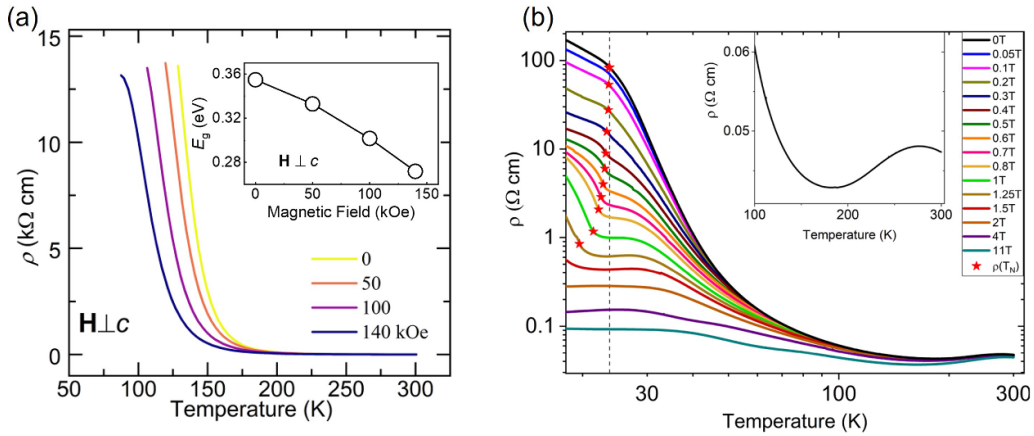

Figure 8. (a) In-plane resistivity of insulating AFM-$EuZn_2P_2$ in different fields transverse to the *c* axis. Inset shows the band gap as a function of the magnetic field. Reprinted figure with permission from [52], Copyright (2023) by the American Physical Society. (b) In-plane resistivity of semiconducting $EuZn_2P_2$ in different fields along the *c* axis. Inset shows the resistivity in zero field above 100 K. Reprinted figure with permission from [33], Copyright (2023) by the American Physical Society.

Analogous to the case of AFM-$EuCd_2As_2$, a resistivity peak at T_N and an increase in resistivity above T_N due to short-range magnetic correlations have been observed. Magnetic fluctuations above T_N are suppressed by applied external fields, leading to a nMR around T_N. Wang *et al*'s data reveal that this nMR peak reaches a maximum of -340% at T_N with an out-of-plane field of 9 T [29]. Figure 7(d) illustrates that Wang *et al*'s sample ($n \sim 8.62 \times 10^{17}$ cm^{-3}) possesses a higher hole concentration compared to Luo *et al*'s ($n \sim 1.42 \times 10^{17}$ cm^{-3}). Despite this difference, the magnitudes of nMR (figures 7(a) and (e)) and the field-dependence of resistivity (figures 7(c) and (f)) are quite similar. Yi *et al* also reported a comparable behavior in $EuZn_2As_2$, albeit with resistivities approximately 700 times greater [55]. Moreover, Blawat *et al* discovered a pronounced angular dependence of MR at a ultralow temperature (0.6 K) and low fields in their $EuZn_2As_2$ crystal ($n \sim 4.6 \times 10^{20}$ cm^{-3}), which led them to claim the presence of field-induced spin reorientation based on their MR analysis [30]. Their recent quantum oscillation studies have further revealed quantum-limited phenomena in $EuZn_2As_2$, suggesting nontrivial topology in its hole bands [60].

Similar to $EuCd_2As_2$ and $EuCd_2P_2$, AFM-$EuZn_2As_2$ also exhibits a significant NLAHE. In Wang *et al*'s work, the NLAHE contributes to 83% of the total Hall resistivity at T_N [29]. Yi *et al* conducted a detailed investigation into the NLAHE in $EuZn_2As_2$, attributing the nonzero Berry curvature to the existence of FM short-range correlations [55]. Their results from electron spin resonance measurements reveal that this short-range FM order persists below T_N. The interplay between the long-range AFM order and the short-range FM order might explain the additional shoulder feature observed in the NLAHE curve below 12 K [55].

5.2.4. Resistivity of AFM-$EuZn_2P_2$. The resistivity data for AFM-$EuZn_2P_2$, as reported by Singh *et al* and Krebber *et al*, are depicted in figures 8(a) and (b), respectively [33, 52]. Initially, $EuZn_2P_2$ was characterized as an insulator exhibiting A-type AFM ordering at 23.5 K. According to the Arrhenius model, the compound displays an energy band gap of approximately 0.2–0.3 eV under the zero-field condition [32, 52]. In line with theoretical predictions and paralleling the behavior of other AFM-EuM_2X_2 compounds [28], the gap narrows when the spins are realigned by an external field, as illustrated in the inset of figure 8(a). Despite this narrowing, the insulating behavior in $EuZn_2P_2$ persists even under fields as high as 14 T. Recently, Krebber *et al* succeeded in synthesizing semiconducting $EuZn_2P_2$ using a graphite crucible, and the resistivity curves are displayed in figure 8(b) [33]. At 100 K, the resistivity of their crystals is roughly six orders of magnitude lower than previously reported values, indicating unintentional heavy doping. Above 200 K, a metallic-like temperature dependence emerges, accompanied by a CMR of $-10^3\%$ at T_N under a 4 T field.

5.3. Pressure effect

Pressure is a powerful tool for modulating electronic states. Several theoretical and experimental investigations have been carried out on EuM_2X_2 materials, with a predominant focus on $EuCd_2As_2$ [31, 50, 61–67]. Gati *et al* and Du *et al* conducted hydrostatic pressure (up to 2.5 GPa) studies utilizing $EuCd_2As_2$ crystals with a bad metal behavior, indicative of a relatively high carrier concentration. Their findings were similar [61, 66]. Primarily, the ground state of $EuCd_2As_2$ transitions from A-type AFM order, featuring in-plane spins (AFM_{ab}), to FM order, also with in-plane spins (FM_{ab}), at a critical pressure of 2 GPa. The phase diagram from Gati *et al* is shown in figure 9(a). This AFM-to-FM transition under pressure underscores the existence of FM interactions in AFM-$EuCd_2As_2$, consistent with experimental observations reported elsewhere. Furthermore, the T_C rises with increasing pressure, suggesting an enhancement of FM coupling. In addition, the low-temperature resistivity exhibits a rapid increase under pressure when $EuCd_2As_2$ is in its

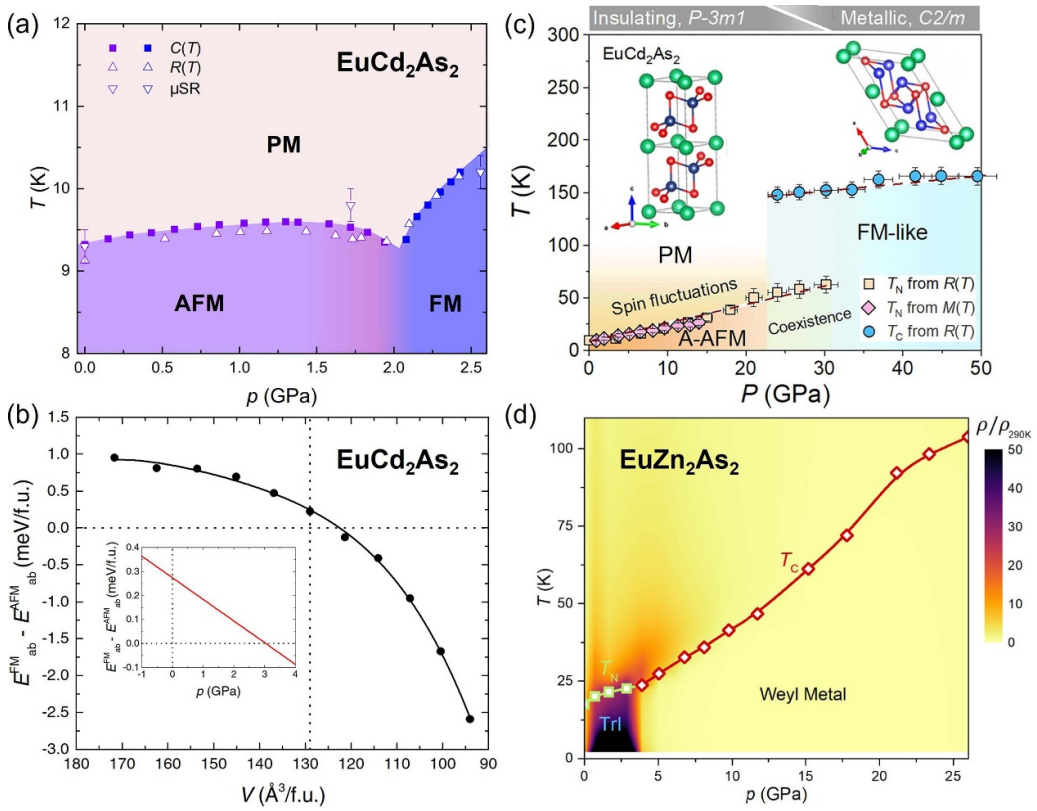

Figure 9. (a) Temperature–pressure (T–p) phase diagram of $EuCd_2As_2$. Reprinted figure with permission from [61], Copyright (2021) by the American Physical Society. (b) Equation of state energy difference vs volume (V) between the fully relaxed FM and A-type AFM states ($E_{FM,ab} - E_{AFM,ab}$), where in both cases the moment point is in-plane to the nearest-neighbor Eu. The inset shows an enlarged view around the AFM_{ab}-to-FM_{ab} transition region with the x axis converted to pressure (p). Reprinted figure with permission from [61], Copyright (2021) by the American Physical Society. (c) T–p phase diagram for intrinsically insulating AFM-$EuCd_2As_2$. Reprinted figure with permission from [50], Copyright (2023) by the American Physical Society. (d) T–p phase diagram of $EuZn_2As_2$ at zero field, where the values of the normalized resistivity are color-coded. The empty rectangles and diamonds respectively represent T_N and T_C (determined from the local maxima in $d\rho/dT$). Reprinted figure with permission from [31], Copyright (2023) by the American Physical Society.

AFM state, reverting to metallic behavior upon transformation into the FM state. Hence, the resistivity forms an insulating dome under intermediate pressures ranging from approximately 1.0–2.0 GPa, accompanied by a CMR effect up to -10^5% upon application of a magnetic field in this pressure region [66]. Simultaneously, T_N undergoes a subtle variation, initially rising before declining. The changes in resistivity and T_N imply alterations to the electronic structures. Lastly, Gati *et al*'s calculations under pressure suggest FM_{ab} state becomes favored with decreasing cell volume, as shown in figure 9(b). Upon further pressure escalation, the FM_{ab} state evolves into a FM state with spins aligned along the c axis (FM_c), with their calculations proposing a critical pressure of 23 GPa for this transformation [61].

Yu *et al* also conducted a pressure study, extending the pressure range up to 30 GPa [63]. Their findings corroborate the AFM-to-FM transition under pressure, enriching the phase diagram established by Gati *et al* and Du *et al* [61, 66]. Notably, T_C of $EuCd_2As_2$ reaches about 30 K at a pressure of 10 GPa. Moreover, Yu *et al* observed a butterfly-shaped MR curve at pressures exceeding 25 GPa, attributed to the magnetic hysteresis of $EuCd_2As_2$ in the FM state [63]. And they claimed a FM_c state at fields above 19 GPa. It is noteworthy that the $EuCd_2As_2$ samples used by Yu *et al* appear to be more semiconducting compared to those in the experiments by Gati *et al*'s and Du *et al*'s experiments [61, 63, 66]. Subsequently, Jose *et al* contributed an additional phase diagram, encompassing pressures up to 42.8 GPa [65]. At this extreme pressure, the T_C value determined via time-domain synchrotron Mössbauer spectroscopy exceeds 80 K and the increase in T_C shows no sign of saturation. Contrary to Gati *et al*'s prediction [61], Jose *et al* discovered that the magnetic moments predominantly orient within the *ab* plane, even at pressures as high as 42.8 GPa [65].

Chen *et al* carried out another high-pressure study on $EuCd_2As_2$, pushing the pressure envelope to 50 GPa [50], as illustrated in figure 9(c). A distinguishing feature of their work is the use of an intrinsically insulating sample for experimentation. Intriguingly, they discovered that the AFM_{ab} state endures up to 30 GPa, beyond which a FM-like state emerges at pressures above 24 GPa. Remarkably, this FM-like state exhibits a T_C reaching 150 K at 24.0 GPa, which increases linearly with pressure at a rate of 0.69 K GPa^{-1}. Additionally, Chen *et al* observed a novel structural transition in $EuCd_2As_2$

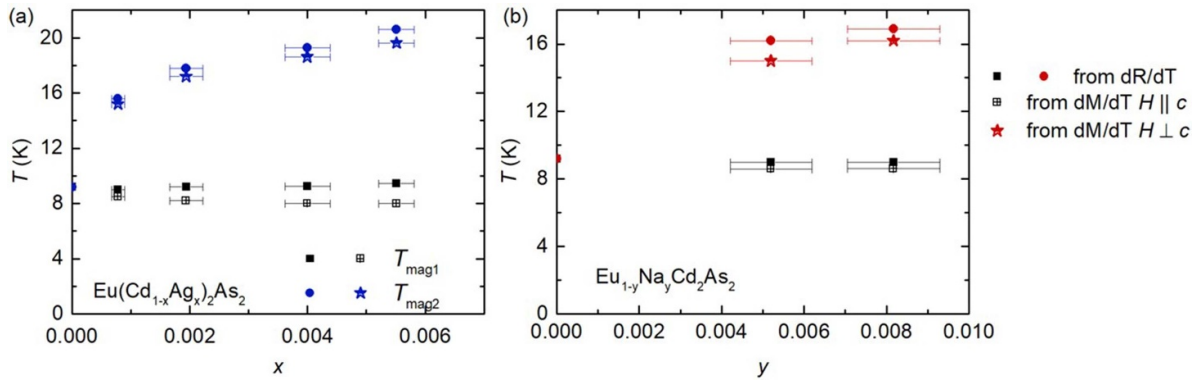

Figure 10. Temperature-doping (T–x) phase diagrams for Ag-substituted $EuCd_2As_2$ (a) and Na-substituted $EuCd_2As_2$ (b). The two magnetic transitions, T_{mag1} and T_{mag2}, are obtained from dM/dT and dR/dT. Reprinted figure with permission from [68], Copyright (2023) by the American Physical Society.

from the P-3m1 to the $C2/m$ space group above 28.2 GPa [50], which is unprecedented in previous studies. The discrepancies between Chen *et al*'s findings and prior research might suggest that carrier density plays an important role in the establishment of FM order. This is reminiscent of the FM-EuM_2X_2 compounds synthesized via the salt flux method [36, 38, 39], which will be elaborated on in section 6.

The magnetic and transport properties of $EuZn_2As_2$ under high pressure have been investigated by Luo *et al* [31]. Analogous to $EuCd_2As_2$, the application of moderate pressure renders $EuZn_2As_2$ increasingly insulative, leading to a huge CMR. Upon reaching a pressure of 4 GPa, $EuZn_2As_2$ undergoes a transition from an AFM semiconductor to a FM metal. The temperature–pressure phase diagram elucidated by Luo *et al* is depicted in figure 9(d). T_C for $EuZn_2As_2$ in the FM state reaches 100 K under a pressure of 26.1 GPa, which is anticipated to increase further under higher pressures. Moreover, Rybicki *et al*'s investigation on $EuZn_2P_2$ shows that the energy gap is markedly suppressed by pressure, resulting in an insulator-to-metal transition [67]. They also documented a substantial rise in T_N, surpassing 40 K at a field of 9.5 GPa. It is noteworthy that the T_N values reported by Rybicki *et al* at elevated pressures might actually represent T_C values [67], as observed in other high-pressure studies.

The high-pressure investigations reveal that the pressure-induced FM order is a pervasive characteristic across the EuM_2X_2 compounds. The magnetic properties under pressure appear to be intimately linked to the intrinsic carrier density within the crystal lattice. On the basis of the aforementioned studies, it appears that $EuZn_2As_2$ and $EuZn_2P_2$ exhibit a higher T_C than $EuCd_2As_2$ at comparable pressures. This observation can be attributed to the reduced cell volumes of the Zn analogs, aligning with the T_C trends observed in FM-EuM_2X_2 compounds synthesized through the salt flux method [38]. To further elucidate these phenomena, future research calls for additional controlled experiments under high pressure on EuM_2X_2 materials. These experiments should explore the effects of varying carrier densities and initial ground states to address outstanding questions and refine our understanding of the underlying mechanisms.

5.4. Doping effect in AFM-$EuCd_2As_2$

To our knowledge, only two instances of intentional heterovalent doping in $EuCd_2As_2$ have been reported thus far: Kuthanazhi *et al* utilized Na^+ and Ag^+ substitutions to introduce hole carriers [68], whereas Nelson *et al* employed La^{3+} substitution to generate extra electrons [69]. Despite endeavors to increase the carrier concentration by enhancing the initial ratio of dopant elements, the achieved doping levels remain fairly low. For instance, a nominal 20% Na content in the starting mixture ($Eu_{0.8}Na_{0.2}Cd_2As_2$) yields a mere 0.8% effective doping ($Eu_{0.992}Na_{0.008}Cd_2As_2$), a situation similarly encountered with Ag substitution at Cd sites and La substitution at Eu sites. These difficulties in doping may stem from the hexagonal close-packed structure of EuM_2X_2 compounds coupled with their high bonding energies.

Kuthanazhi *et al* observed a splitting of the original AFM transition in $EuCd_2As_2$ into two distinct transitions [68]. The lower transition, labeled as T_{mag1}, is independent of doping, whereas the higher transition, denoted as T_{mag2}, increase gradually with the increased chemical substitution. This behavior was noted for both Ag- and Na-doped samples, as illustrated in figure 10. The authors found that T_{mag2} is associated with a FM component of moments within the *ab* plane, leading them to posit that a shift in band filling could potentially stabilize a FM phase in $EuCd_2As_2$. This hypothesis is corroborated by their theoretical calculations and aligns with the FM ground state observed in defect-rich EuM_2X_2 compounds. It is noteworthy that, in Kuthanazhi *et al*'s study, the fluctuations in T_{mag2} and the Weiss temperatures (θ_W), indicators of FM interaction strength, are modest, even as the chemical doping level varies by an order of magnitude [68]. This observation may suggest that carrier concentration is not the predominant determinant of FM correlation strength, which will be revisited in section 6.2.2.

Nelson *et al* prepared n-type $EuCd_2As_2$ crystals through La doping at Eu sites, achieving a dopant concentration of 30 ppm and a doping level about 10^{17} cm^{-3} [69]. Their ARPES measurements, performed at 6 K on potassium-dosed samples, unveiled a clear band gap for AFM-$EuCd_2As_2$. This finding

provides strong evidence supporting the recent reports of semiconducting behavior in $EuCd_2As_2$ by Santos-Cottin *et al*, as previously introduced [25].

Although heterovalent doping is challenging in EuM_2X_2, it holds promise as a method for controlling carrier concentration and tuning the physical properties of these materials, warranting further exploration.

6. Physical properties of FM-EuM_2X_2

Recent investigations have demonstrated that all four compounds in the EuM_2X_2 series (M = Zn, Cd; X = P, As), which exhibit a FM ground state, can be synthesized using the salt flux method. This section aims to delineate the magnetic and transport properties of these FM-EuM_2X_2 materials and to discuss the mechanisms underlying the interlayer FM couplings.

6.1. FM-$EuCd_2As_2$

6.1.1. Magnetism and resistivity. Initial interest in $EuCd_2As_2$ in a FM state was sparked by theoretical predictions that its out-of-plane ferromagnetism, i.e., the c-axis polarized spin state, can host an idea WSM phase with a single pair of Weyl nodes [11, 13, 14]. However, while FM correlations are detected above and below T_N (9.5 K) in AFM-$EuCd_2As_2$ [10, 53], no net FM component is discernible when the long-range AFM order is established. Surprisingly, Jo *et al* managed to synthesize FM-$EuCd_2As_2$ with an ordering temperature of 26 K merely by altering the flux from Sn to a mixture of NaCl and KCl [36]. This represents a rare case of effectively manipulating the ground state of a material through such a simple modification.

Figures 11(a)–(c) summarize the magnetization data for AFM- and FM-$EuCd_2As_2$. Jo *et al* found that both AFM and FM variants of $EuCd_2As_2$ can be synthesized using the salt flux method, contingent upon the concentration of Eu in the solution. Interestingly, the magnetic properties, encompassing the T_N values and the saturation fields, of AFM-$EuCd_2As_2$ crystals grown via the salt flux technique align closely with those grown using the Sn flux method. All $EuCd_2As_2$ samples exhibit an easy-plane magnetic anisotropy, signifying that the Eu spins lie in the ab plane. It is worth noting that the saturation field of FM-$EuCd_2As_2$ for H // ab is noticeably reduced, indicating a pronounced enhancement of the FM coupling between the Eu layers. This analogous decrease in saturation field under in-plane fields is also observed in other FM-EuM_2X_2 compounds, which will be elaborated in section 6.2.1. The specific heat and resistivity derivative collectively substantiate the bulk FM transition in FM-$EuCd_2As_2$, rather than signaling a mere FM component arising from a canted AFM order. Additional corroborative evidence, such as the direct visualization of FM domains through magneto-optical imaging, further attests to the presence of FM order in FM-$EuCd_2As_2$. High-energy x-ray diffraction experiments, along with benchtop x-ray techniques, have revealed a slight deficiency in Eu content (approximately 1% to 4%). This Eu deficiency is believed to play a critical role in a band shift of the hole pocket, thereby affecting the material's ground state properties.

Roychowdhury *et al* studied the charge transport of FM-$EuCd_2As_2$ under various magnetic fields, as shown in figure 11(f) [37]. The material exhibits metallic conductivity, with the exception of an upturn observed above the T_C of FM ordering. Moreover, the transition peak at 26 K is rapidly suppressed by applied fields, resulting in a pronounced nMR effect.

6.1.2. Doping effect. Theoretical calculations by Wang *et al* predicted that replacing half of the Eu atoms with Ba in AFM-$EuCd_2As_2$ would induce a lattice expansion, thereby stabilizing a FM ground state with an out-of-plane spin configuration [13]. To test this hypothesis, Sanjeewa *et al* synthesized a series of $Eu_{1-x}Ba_xCd_2As_2$ single crystals using the salt flux method, with Ba doping concentrations ranging from 0% to 40% [70]. The magnetization data for these crystals are presented in figure 12. The splitting of zero-field-cooled (ZFC) and field-cooled (FC) data, alongside the markedly enhanced in-plane susceptibility, unambiguously signals the in-plane FM order in the Ba-doped samples, in agreement with the findings reported by Jo *et al* [36]. Several key observations merit attention:

Firstly, with low Ba substitution levels, T_C remains almost invariant; however, a significant decline in T_C is observed at higher doping concentrations, indicative of a weakening in the FM coupling strength.

Secondly, contrary to expectations of monotonic evolution, the susceptibility magnitude initially decreases before reverting to the value of the parent compound, suggestive of non-monotonic change in the spin canting angle.

Thirdly, the authors did not detect any Eu vacancies in their undoped FM-$EuCd_2As_2$, contradicting earlier reports [36]. Yet, a subtle carrier concentration shift can provoke substantial alterations in the magnetism of EuM_2X_2 compounds, potentially exceeding the detection limits of the experimental apparatus.

Fourthly, the theoretical prediction that Ba doping induces ferromagnetism in $EuCd_2As_2$ could not be confirmed in this study, as the parent compound was already FM. To properly assess this prediction, semiconducting $EuCd_2As_2$ should be serve as the parent material.

6.2. FM-$EuCd_2P_2$, FM-$EuZn_2P_2$, and FM-$EuZn_2As_2$

6.2.1. Magnetism. The aforementioned results clearly demonstrate that FM-$EuCd_2As_2$ was successfully synthesized using the salt flux method. The alteration in its magnetic ground state is attributed to the reduced Eu^{2+} content and the consequent shift in the Fermi level. Given that other members of the EuM_2X_2 family share the $CaAl_2Si_2$-type structure, exhibit an A-type AFM configuration, and display similar short-range FM correlations, it is logical to explore the potential for discovering additional FM compounds within

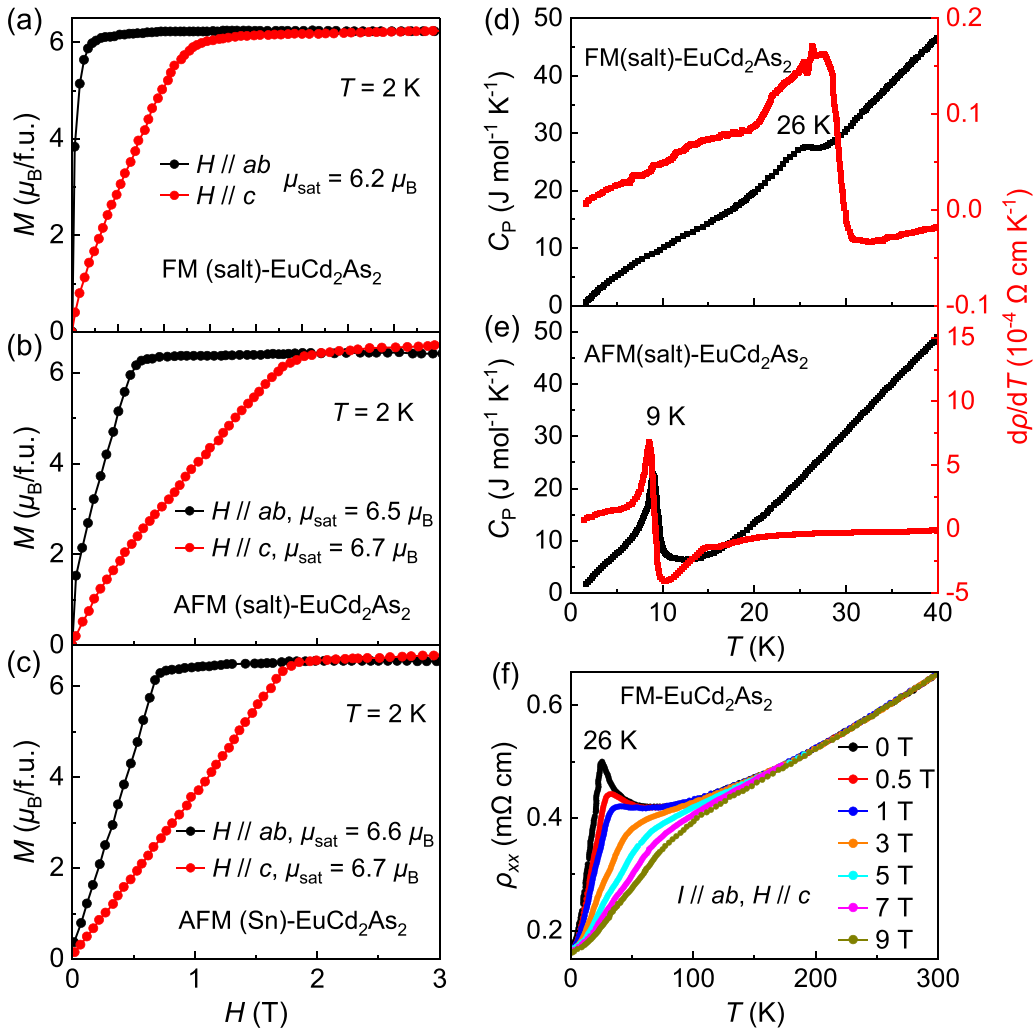

Figure 11. (a)–(c) Field-dependent magnetization with in-plane (H // ab) and out-of-plane (H // c) fields at 2 K for FM-$EuCd_2As_2$, salt flux grown AFM-$EuCd_2As_2$, and Sn flux grown AFM-$EuCd_2As_2$, respectively. (d)–(e) Temperature-dependent specific heat C_P (black line, left axis) and resistivity derivatives dρ/dT (red line, right axis) for FM-$EuCd_2As_2$ and AFM-$EuCd_2As_2$, respectively. Panels (a)–(e) Reprinted figure with permission from [36], Copyright (2020) by the American Physical Society. (f) Temperature-dependent of resistivity for FM-$EuCd_2As_2$ under various fields. Panel (f) [37]. John Wiley & Sons. © 2023 Wiley-VCH GmbH.

this family. Indeed, our recent investigations have revealed that FM single crystals of $EuZn_2P_2$ (T_C = 72 K), $EuZn_2As_2$ (T_C = 42 K), and $EuCd_2P_2$ (T_C = 47 K) can also be grown utilizing the salt flux technique [38, 39].

Figure 13 shows the susceptibility (H // c) and magnetization (H // ab and H // c) of the FM variants of $EuZn_2P_2$, $EuZn_2As_2$, and $EuCd_2P_2$. Clear bifurcations in the FC and ZFC data, the significant increase around T_C, and the presence of magnetic hysteresis loops unequivocally confirm the FM ground state in these three materials. This contrasts with the sharp peak characteristic of AFM phases at T_N and their non-hysteretic magnetization behaviors. The T_C values were determined through the derivative of the susceptibility, $d\chi_c/dT$, yielding results of 72 K for FM-$EuZn_2P_2$, 42 K for FM-$EuZn_2As_2$, and 47 K for FM-$EuCd_2P_2$. The in-plane magnetization curves for all three compounds display a pronounced hysteresis effect, whereas the out-of-plane hysteresis loops are notably weak, suggesting that the magnetic easy axis lies within the ab plane. Furthermore, the in-plane saturation fields for the FM-EuM_2X_2 series are markedly lower when compared to those depicted in the bottom panels of figure 3, indicating a substantially enhanced FM coupling between the Eu planes. Additionally, the Weiss temperatures (θ_W) obtained from fitting (78.8 K for FM-$EuZn_2P_2$, 49.2 K for FM-$EuZn_2As_2$, 50.2 K for FM-$EuCd_2P_2$) are closely aligned with the respective T_C values, which further supports the conclusion that $EuZn_2P_2$, $EuZn_2As_2$, and $EuCd_2P_2$ are intrinsic ferromagnets rather than canted antiferromagnets.

Base on the single-crystal x-ray diffraction data, the crystal structures of FM-EuM_2X_2 are virtually identical to those of their AFM counterparts, except for a slight proportion of Eu vacancies in the FM phases (∼5% for FM-$EuZn_2P_2$, ∼0.2% for FM-$EuCd_2P_2$) [38, 39], reminiscent of the situation observed in $EuCd_2As_2$. We have previously discussed that AFM interactions in EuM_2X_2 family is mediated by the superexchange mechanism via the Eu–X–X–Eu path [52]. Given

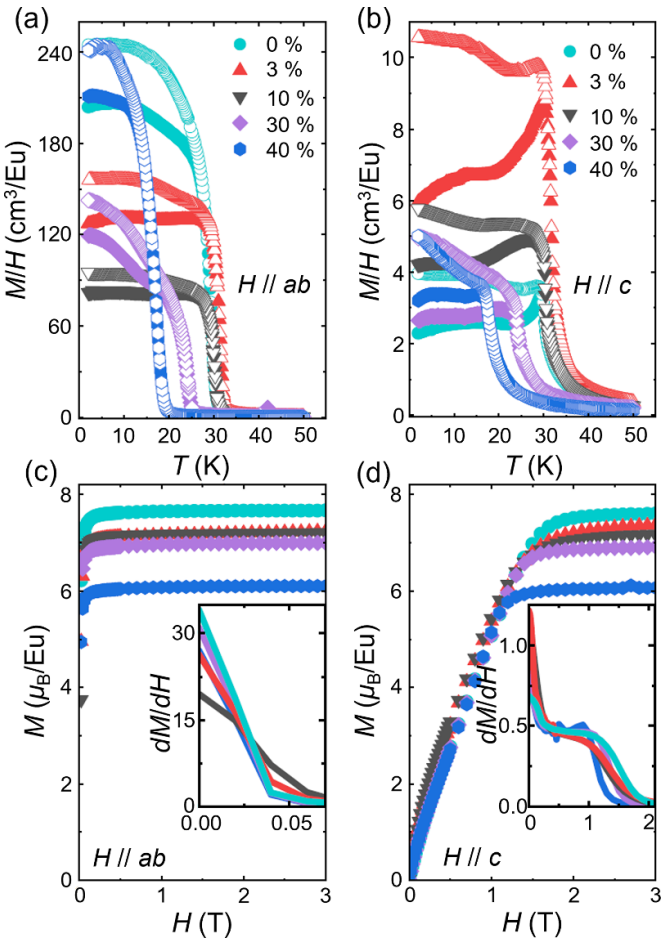

Figure 12. Temperature-dependent magnetization of $Eu_{1-x}Ba_xCd_2As_2$ with a field of 50 Oe applied (a) in the *ab* plane and (b) along the *c* axis. Closed symbols represent ZFC data, and open symbols represent FC data. Magnetization field sweeps for field applied (c) in-plane and (d) along the *c* axis. Insets in (c) and (d) show the field derivative (d*M*/d*H*) for the two field orientations. Reprinted figure with permission from [70], Copyright (2020) by the American Physical Society.

that the Eu–*X* and *X*–*X* bond lengths and Eu–*X*–*X* bond angles remain essentially constant, it is reasonable to infer that the interlayer AFM interaction persists. Therefore, the emergent ferromagnetism must stem from an enhancement of interlayer FM coupling, which now dominates, a condition that can only be attributed to the presence of low-concentration hole carriers. The induction of ferromagnetism by a low carrier concentration is not exclusive to the EuM_2X_2 series. Precedents abound, including FM semiconductors EuX (X = O, S, Se, Te) [71, 72], the diluted magnetic semiconductor (Ga,Mn)As [73, 74], the Mn pyrochlore $Tl_{2-x}Sc_xMn_2O_7$ [75], and other low-carrier-density ferromagnets such as $Ca_{1-x}La_xB_6$, EuB_6, UTeS, PbSnMnTe, etc [76–79].

6.2.2. Characteristic temperatures of EuM_2X_2. FM-$EuZn_2P_2$ attains a remarkably high T_C of 72 K among Eu-based materials, nearly three times that of FM-$EuCd_2As_2$, which has a T_C of 26 K. This raises the natural question of what factors critically determine the magnitude of T_C. The characteristic temperatures (T_C, T_N, θ_W) for both FM- and AFM-EuM_2X_2 are plotted in figure 14, as a function of the Eu-layer distances (d_{inter}), i.e. the *c*-axis values listed in table 1. Surprisingly, it is discovered that both the FM transition temperature T_C and the Weiss temperature θ_W exhibit a linear correlation with the interlayer distance. This linear dependence strongly suggests that the FM ordering temperatures of the FM-EuM_2X_2 series are heavily reliant on the strength of interlayer Eu–Eu coupling. It is not unexpected that such a linear relationship does not hold in the AFM phases, given the distinct mechanisms governing AFM interactions. Moreover, we observe that the T_C values are consistently somewhat lower than their corresponding θ_W. This disparity can likely be attributed to the existing influence of AFM interactions. Consequently, it is unsurprising to find a greater divergence between T_C and θ_W for FM-$EuZn_2P_2$ and FM-$EuZn_2As_2$, owing to their shorter Eu–*X*–*X*–Eu path.

Another critical aspect that requires discussion is the role of carrier densities. It has been established that the hole carriers, induced by Eu vacancies, play a crucial role in the establishment of FM order. However, unlike the scenario observed in electron-doped FM semiconductors EuX (X = O, S, Se) [80–82], the final T_C appears not to be significantly impacted by variations in carrier density. This inference is backed by several observations. Firstly, T_C values reported for FM-$EuCd_2As_2$ across various research groups exhibit good consistency [36, 37, 70]. Secondly, our attempts to grow EuM_2X_2 crystals under differing flux concentrations resulted in virtually unaltered T_C values. Thirdly, as previously discussed, the T_C of FM-$EuCd_2As_2$ derived from heterovalent doping does not exhibit a pronounced dependency on the doping concentration [68]. These insights suggest the existence of a threshold concentration of Eu vacancies necessary for the carrier-induced transition from AFM to FM order. For instance, the carrier concentration of FM-$EuCd_2P_2$ ($\sim 4.6 \times 10^{19}$ cm^{-3}, equivalent to 0.26% Eu vacancy/f.u.) is about an order of magnitude higher than that of AFM-$EuCd_2P_2$ (3.6×10^{18} cm^{-3}, equivalent to 0.02% Eu vacancy/f.u.) [38, 39]. The threshold concentration falls somewhere between these two values. Once the hole concentration surpasses this threshold, EuM_2X_2 transitions into the FM state with a characteristic T_C, without manifesting any intermediate magnetic phase. This threshold warrants further investigation, given the current inability to continuously modulate the Eu vacancy concentration in samples using the Sn or salt flux growth methods. Future theoretical and experimental efforts should be devoted to elucidating the precise impact of carrier density on T_C and T_N.

6.2.3. Charge transport. The holes induced by Eu vacancies not only alter the magnetic order of EuM_2X_2 compounds, but also dramatically decrease their resistivity. The charge transport properties of FM-$EuZn_2P_2$ and FM-$EuCd_2P_2$ are illustrated in figure 15, whereas data for FM-$EuZn_2As_2$ are omitted due to the inferior crystal quality, which hindered the data

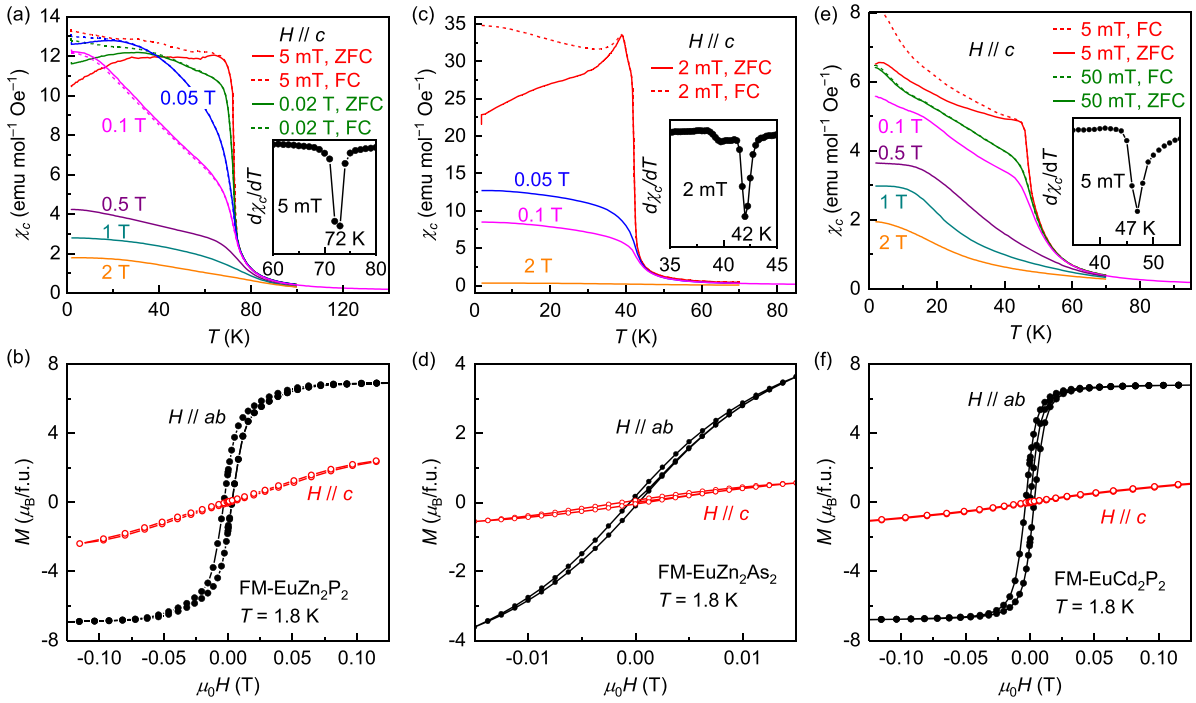

Figure 13. Temperature-dependent susceptibility and magnetic hysteresis loops of FM-$EuZn_2P_2$ ((a), (b)), FM-$EuZn_2As_2$ ((c), (d)), and FM-$EuCd_2P_2$ ((e), (f)) under various conditions. The insets in panels (a), (c), and (e) depict the transition temperatures as determined by the derivative of the susceptibility data. (a)–(d) Reprinted figure with permission from [38], Copyright (2024) by the American Physical Society. (e)–(f) Reprinted figure with permission from [39], Copyright (2024) by the American Physical Society.

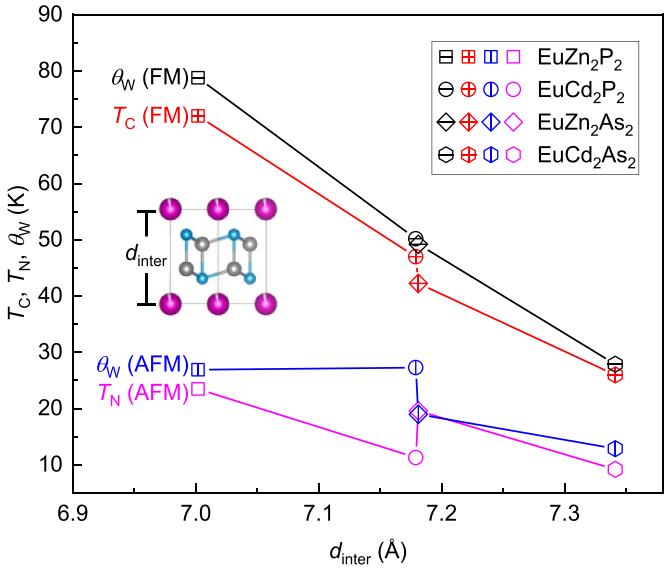

Figure 14. The characteristic temperatures (T_C, T_N, θ_W) of EuM_2X_2 (M = Zn, Cd; X = P, As) as a function of the Eu-layer distance, i.e., the c axis. The squares, circles, diamonds, and hexagons represent the data of FM $EuZn_2P_2$, $EuCd_2P_2$, $EuZn_2As_2$, and $EuCd_2As_2$, respectively. Reprinted figure with permission from [38], Copyright (2024) by the American Physical Society.

collection. In stark contrast to the AFM counterparts, both FM-$EuZn_2P_2$ and FM-$EuCd_2P_2$ display metallic behavior, accompanied by a resistivity peak at T_C. By applying the magnetic field, magnetic scatterings are significantly diminished, resulting in the rapid suppression of the resistivity peak and the manifestation of a pronounced nMR effect around T_C. Panel (b) depicts the field-dependent resistivity, of FM-$EuZn_2P_2$ at various temperatures, while the calculated MR as a function of field for FM-$EuCd_2P_2$ is displayed in panel (e). A slight rise in $\rho(H)$ and MR(H) was observed under low fields when the temperatures are well below T_C, attributed to the enhanced canting of spins toward the c axis in the field. Panel (c) plots the normalized resistivity of FM-$EuZn_2P_2$, ρ(H)/ρ(0 T), at 72 K (T_C), 85 K (1.2 T_C), and 130 K (1.8 T_C) versus normalized magnetization (M/M_{sat}). The consistent trend across the three datasets suggests that the MR of FM-$EuZn_2P_2$ is closely tied to its magnetization, signifying that magnetic scattering is a predominant factor in the MR effect. By plotting $-\Delta\rho/\rho(0\ \mathrm{T})$ as a function of $(M/M_{sat})^2$, we discerned that their relationship could be described by the scaling function $-\Delta\rho/\rho(0\ \mathrm{T}) = C(M/M_{sat})^2$ [83]. The derived coefficient C is consistent with the prediction of the Majumdar–Littlewood model [38]. Hence, the nMR of FM-$EuZn_2P_2$ can potentially be augmented merely by reducing the carrier concentration.

In addition, FM-$EuCd_2P_2$ exhibits a hump in resistivity around 30 K, which is notably absent in other FM-EuM_2X_2 materials. This anomaly may stem from the competition between short-range magnetic correlations and interlayer FM coupling below T_C, given the pronounced magnetic fluctuations in AFM-$EuCd_2P_2$ and the subtle modifications to the crystal structure upon transitioning between the two phases. Figure 15(f) presents the contrasting resistivity magnitudes of the AFM- and FM-$EuCd_2P_2$. The striking disparity in the

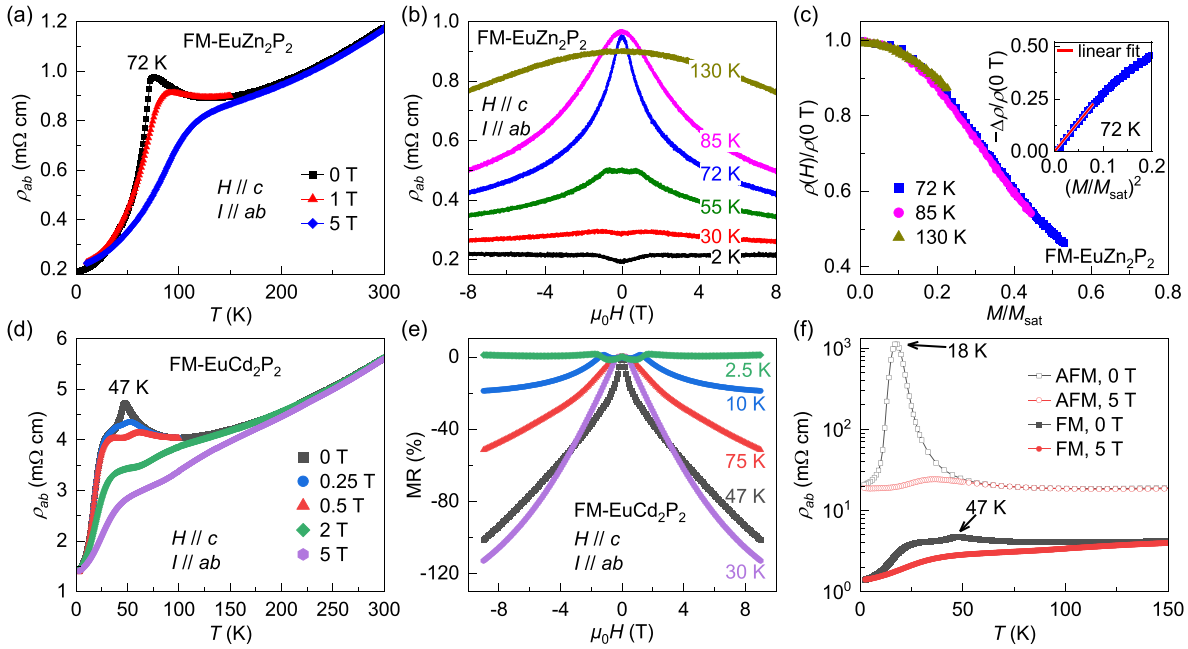

Figure 15. Electrical transport data of FM-$EuZn_2P_2$ and FM-$EuCd_2P_2$. (a) In-plane resistivity of FM-$EuZn_2P_2$ under several fields along the c axis. (b) Field-dependent resistivity at various temperatures from 2 to 130 K. (c) Normalized resistivity $\rho(H)/\rho(0\ \mathrm{T})$ at 72 K (blue squares), 85 K (magenta circles), and 130 K (dark yellow triangles) plotted against normalized field-induced magnetization M/M_{sat}, where M_{sat} is the saturated magnetization. (a)–(c), Reprinted figure with permission from [38], Copyright (2024) by the American Physical Society. (d) In-plane resistivity of FM-$EuCd_2P_2$ under several fields along the c axis. (e) Calculated MR of FM-$EuCd_2P_2$ as a function of field at several representative temperatures. (f) A comparison of the resistivity behaviors between AFM- and FM-$EuCd_2P_2$. Note that the resistivity is plotted on a logarithmic scale. (d)–(f) Reprinted figure with permission from [39], Copyright (2024) by the American Physical Society.

resistivity behavior and magnetic properties between the AFM and FM states, coupled with the subtle alteration in carrier density, positions $EuCd_2P_2$ as a promising candidate for future spintronic applications.

7. Conclusion and perspectives

This work offers a comprehensive review of EuM_2X_2 (M = Zn, Cd; X = P, As) materials, delving into their crystal structure, magnetic properties, electrical transport characteristics, and electronic structure in detail. The initial impetus for studying EuM_2X_2 stemmed from the theoretical prediction of a WSM state in $EuCd_2As_2$, although this concept has faced significant scrutiny. Nevertheless, meticulous exploration of EuM_2X_2 properties has unveiled a rich landscape ripe with exotic phenomena such as the NLAHE, CMR effect, and highly modifiable magnetic and electrical transport behaviors. From a practical standpoint, the tunable properties of EuM_2X_2 materials make them exceptionally promising candidates for spintronic applications. Our review concludes with several key takeaways:

(a) *EuM_2X_2 (M = Zn, Cd; X = P, As) are most likely magnetic semiconductors lacking a topologically nontrivial nature.* Previous claims designating $EuCd_2As_2$ primarily relied on theoretical calculations and experiments involving heavily p-doped $EuCd_2As_2$ samples. These claims have been systematically challenged by recent meticulous theoretical studies and experiments conducted on ultraclean or n-doped $EuCd_2As_2$ crystals [25–28]. Indeed, experimental phenomena once attributed to Weyl physics, such as the giant NLAHE, could be accounted for by alternative mechanisms [16, 55].

(b) *Despite hosting an A-type AFM order, FM correlations predominate within the EuM_2X_2 family.* This peculiar confluence engenders a constellation of distinctive properties across EuM_2X_2 compounds, including strong FM fluctuations, the CMR effect, the NLAHE, carrier-induced FM ordering, and pressure-induced FM ordering. Furthermore, the intensity of FM interactions is intimately tied to the dimensions of the unit cell, as evidenced by the T_C trends observed in EuM_2X_2 synthesized via the salt flux method [36, 38], and the enhancement of T_C under elevated pressures [31, 50, 65].

(c) *The narrow band gap and its sensitivity to the spin configurations jointly contribute to the highly tunable charge transport properties in EuM_2X_2.* Reported modulation techniques encompass the application of magnetic field, pressure, bias currents [27], carrier doping, and strain [62, 64], etc. The high tunability lays the groundwork for the prospective utilization of EuM_2X_2 in various applications.

(d) *A phase diagram is compiled to depict the correlation between carrier concentration and the resultant magnetism and charge transport characteristics in EuM_2X_2 compounds.* As shown in figure 16, three distinct regions emerge: a yellow-shaded area signifies AFM semiconducting phases of EuM_2X_2, characterized by an exceedingly low hole density (typically below 10^{17} cm^{-3}) and a pronounced

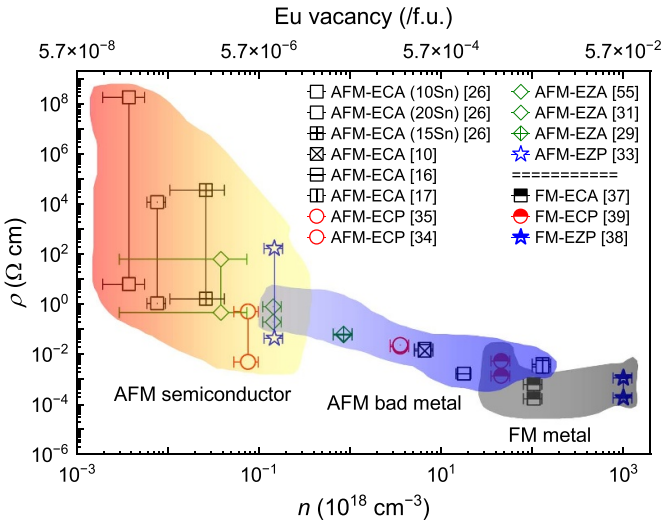

Figure 16. The upper bound and lower bounds of resistivity for EuM_2X_2 compounds, plotted as a function of the carrier densities (bottom axis). Corresponding value of Eu vacancy is indicated on the top axis. Each distinct symbol represents a compound in either the AFM or FM ground state. Resistivity for each phase is denoted by dual data points, which represent the maximum and minimum values extracted from the resistivity curves without the field. Carrier densities were calculated using the OHE contributions from the Hall resistivity curves. The horizontal error bars are estimated based on the variability of carrier density across different temperatures. Where Hall data at multiple temperatures are unavailable, an error bar equivalent to 25% of the carrier density is assumed. ECA, ECP, EZA, and EZP designate the compounds $EuCd_2As_2$, $EuCd_2P_2$, $EuZn_2As_2$, and $EuZn_2P_2$, respectively. The sources of the data are denoted within the figure.

shift in resistivity magnitude. A blue-shade area signifies EuM_2X_2 exhibiting relatively low resistivity for intermediate carrier densities (ranging approximately from 10^{17} cm^{-3} to 10^{20} cm^{-3}), with a subtle variation in resistivity magnitude, yet maintaining A-type AFM magnetic order. A black-shaded area represents FM-EuM_2X_2 manifesting typical metallic behavior for higher carrier concentrations within the crystal lattice (approximately exceeding 10^{20} cm^{-3}). Note that for the heavily *p*-doped sample with a carrier density of 10^{21} cm^{-3}, the estimated Eu vacancy, based on a single-band model, amounts to merely 0.06 per formula unit. Besides, we notice that the carrier densities of $EuCd_2As_2$, synthesized via different methods, span a broad range of five orders of magnitude, from 10^{15} to 10^{20} cm^{-3}, which accounts for the diverse properties reported in literature for $EuCd_2As_2$. This phase diagram implies that a subtle fluctuation in the concentration of Eu defects could precipitate a dramatic alteration in the magnetic and charge transport properties of *EuM_2X_2* compounds.

In the past few years, considerable research efforts have been dedicated to exploring EuM_2X_2 compounds, yielding significant advancements. However, several outstanding questions still need addressing, and further manipulation of these materials' properties is warranted. Below, we would like to outline some potential research avenues in this specific topic:

(e) *The mechanism by which long-range FM order is established in EuM_2X_2 compounds.* Experimental findings have demonstrated that a modest application of pressure or a slight adjustment in carrier density can induce a switch in the magnetic ground state [38, 61]. However, a comprehensive theoretical framework to explain this mechanism is currently absent. The specific pathway through which interlayer FM coupling is mediated is yet to be elucidated.

(f) *The origins of the giant NLAHE and CMR.* These phenomena are commonly observed in EuM_2X_2 compounds, suggesting a universe physical cause. Although several mechanisms have been postulated for specific materials [16, 42, 55], a comprehensive understanding that encapsulates all members of EuM_2X_2 family has yet to be fully elucidated.

(g) *The continuous modulation of carrier density in EuM_2X_2 compounds.* In section 6.2.2, we posit the existence of a critical carrier density threshold for the transition between AFM and FM state. However, this hypothesis remains unverified, as the salt flux method can not finely tune the carrier density within EuM_2X_2 crystals. Moreover, chemical doping presents significant challenges in this system. Electrostatic gating emerges as a promising solution, suitable not only for EuM_2X_2 thin films [84–86] but also for micrometer-scale single-crystalline lamellae [87]. It would be intriguing to determine whether the T_N and T_C vary continuously with changes in carrier density, or if a sudden jump occurs instead. And it is also of great interest to see the maximum T_C attainable through the modulation of carrier density, which is a critical consideration for the application of EuM_2X_2 in spintronics.

(h) *Enhance T_C of FM-EuM_2X_2 through the reduction of interlayer Eu–Eu distances.* As shown in figure 14 in section 6.2.2, a linear increase in T_C is observed as the interlayer spacing decreases. Moreover, the highest T_C values obtained for $EuCd_2As_2$ through high-pressure studies exceed 150 K at 49.5 GPa [50], whereas the record for $EuZn_2As_2$ stands at 100 K at 26.1 GPa [31]. These findings suggest that T_C could be further enhanced by compressing the unit cell volume via chemical pressure, specifically through doping with ions of smaller size. Substituting Eu sites with small divalent elements, such as Ca^{2+} and Yb^{2+}, could effectively strengthen interlayer FM coupling. However, non-magnetic dopants may conversely diminish magnetic interactions, as evidenced by the T_C trend of $Eu_{1-x}Ba_xCd_2As_2$ [70]. Gd^{3+} is also a viable dopant candidate due to its smaller radius and the same $4f^7$ electron configuration. Moreover, Gd^{3+} allows for the introduction of extra electrons into the lattice to explore the properties of *n*-type EuM_2X_2.

(i) *High-pressure studies involving both insulating and metallic variants of EuM_2X_2.* Previous high-pressure experiments conducted on both insulating and metallic $EuCd_2As_2$ have unveiled notable discrepancies [50, 65]. This discrepancy has yet to be satisfactorily explained. It holds considerable intrigue to probe whether other EuM_2X_2 compounds, characterized by differing carrier densities, might exhibit a spectrum of pressure-induced phenomena. Furthermore, among the quartet, $EuZn_2P_2$ may potentially display the highest T_C under pressure, attributed to its notably shorter interlayer Eu–Eu distance.

(j) *Enhance the CMR effect.* The CMR effect is a pivotal phenomenon due to its critical importance in magnetic memory and sensing technologies. Based on observations of the magnetoresistive responses in EuM_2X_2 compounds, it appears that more insulating behavior correlates with a greater CMR effect. Therefore, enhancing the CMR effect could be achieved through a moderate increase in the energy gap.

(k) *Explore the possibility of manipulating the ground state in other Eu-based materials with a $CaAl_2Si_2$-type structure.* As mentioned in section 2, numerous Eu-based compounds exhibiting an A-type AFM ordering were synthesized previously, such as $EuAl_2Ge_2$ [44], $EuMg_2(Sb/Bi)_2$ [45, 88], $Eu(Zn/Cd)_2Sb_2$ [89, 90], and $EuMn_2X_2$ (X = P, As, and Sb) [4, 46, 91], etc. It would be intriguing to investigate whether FM order could be induced in these materials.

(l) *The peculiar features of $EuCd_2P_2$.* Among the EuM_2X_2 compounds, $EuCd_2P_2$ stands out as particularly distinctive. It exhibits exceptionally strong FM fluctuations. Notably, its resistivity peak is significantly elevated above T_N, with the peak temperature itself being correlated to the carrier density within the sample. Additionally, FM-$EuCd_2P_2$ displays a pronounced resistivity hump around 30 K, as shown in figure 15(d). These anomalous characteristics remain unexplained and warrant further investigative efforts.

In summary, even without a topologically nontrivial nature, the EuM_2X_2 family (M = Zn, Cd; X = P, As) remains a rich field for exploring the intricate interplay between magnetism and transport properties.

Data availability statement

No new data were created or analyzed in this study.

Acknowledgment

This work was supported by the National Natural Science Foundation of China (Grants No. 12204094), the Natural Science Foundation of Jiangsu Province (Grant No. BK20220796), the Start-up Research Fund of Southeast University (Grant No. RF1028623289), the Interdisciplinary program of Wuhan National High Magnetic Field Center (WHMFC) at Huazhong University of Science and Technology (Grant No. WHMFC202205).

ORCID iDs

Xiyu Chen https://orcid.org/0000-0002-8702-5491
Shuai Dong https://orcid.org/0000-0002-6910-6319
Zhi-Cheng Wang https://orcid.org/0000-0003-0100-3900

References

[1] Klüfers P, Neumann H, Mewis A and Schuster H-U 1980 AB_2X_2-verbindungen im $CaAl_2Si_2$-Typ, VIII [1]/AB_2X_2 compounds with the $CaAl_2Si_2$ structure, VIII [1] *Z. Naturforsch.* **35** 1317

[2] Artmann A, Mewis A, Roepke M and Michels G 1996 AM_2X_2-Verbindungen mit $CaAl_2Si_2$-Struktur. XI. Struktur und Eigenschaften der Verbindungen ACd_2X_2 (*A*: Eu, Yb; *X*: P, As, Sb) *Z. Anorg. Allg. Chem.* **622** 679

[3] Schellenberg I, Pfannenschmidt U, Eul M, Schwickert C and Pöttgen R 2011 A ^{121}Sb and ^{151}Eu Mössbauer spectroscopic investigation of $EuCd_2X_2$ (X = P, As, Sb) and $YbCd_2Sb_2$ *Z. Anorg. Allg. Chem.* **637** 1863

[4] Schellenberg I, Eul M, Hermes W and Pöttgen R 2009 A ^{121}Sb and ^{151}Eu Mössbauer spectroscopic investigation of $EuMn_2Sb_2$, $EuZn_2Sb_2$, $YbMn_2Sb_2$, and $YbZn_2Sb_2$ *Z. Anorg. Allg. Chem.* **636** 85

[5] May A F, McGuire M A, Ma J, Delaire O, Huq A and Custelcean R 2012 Properties of single crystalline AZn_2Sb_2 (A = Ca,Eu,Yb) *J. Appl. Phys.* **111** 033708

[6] Zhang H, Zhao J-T, Grin Y, Wang X-J, Tang M-B, Man Z-Y, Chen H-H and Yang X-X 2008 A new type of thermoelectric material, $EuZn_2Sb_2$ *J. Chem. Phys.* **129** 164713

[7] Liu Z K *et al* 2014 A stable three-dimensional topological Dirac semimetal Cd_3As_2 *Nat. Mater.* **13** 677

[8] Rahn M C, Soh J-R, Francoual S, Veiga L S I, Strempfer J, Mardegan J, Yan D Y, Guo Y F, Shi Y G and Boothroyd A T 2018 Coupling of magnetic order and charge transport in the candidate Dirac semimetal $EuCd_2As_2$ *Phys. Rev.* B **97** 214422

[9] Wang H P, Wu D S, Shi Y G and Wang N L 2016 Anisotropic transport and optical spectroscopy study on antiferromagnetic triangular lattice $EuCd_2As_2$: an interplay between magnetism and charge transport properties *Phys. Rev.* B **94** 045112

[10] Ma J-Z *et al* 2019 Spin fluctuation induced Weyl semimetal state in the paramagnetic phase of $EuCd_2As_2$ *Sci. Adv.* **5** eaaw4718

[11] Soh J-R *et al* 2019 Ideal Weyl semimetal induced by magnetic exchange *Phys. Rev.* B **100** 201102(R)

[12] Ma J *et al* 2020 Emergence of nontrivial low-energy Dirac fermions in antiferromagnetic $EuCd_2As_2$ *Adv. Mater.* **32** 1907565

[13] Wang L-L, Jo N H, Kuthanazhi B, Wu Y, McQueeney R J, Kaminski A and Canfield P C 2019 Single pair of Weyl fermions in the half-metallic semimetal $EuCd_2As_2$ *Phys. Rev.* B **99** 245147

[14] Hua G, Nie S, Song Z, Yu R, Xu G and Yao K 2018 Dirac semimetal in type-IV magnetic space groups *Phys. Rev.* B **98** 201116(R)

[15] Taddei K M, Yin L, Sanjeewa L D, Li Y, Xing J, Dela Cruz C, Phelan D, Sefat A S and Parker D S 2022 Single pair of Weyl nodes in the spin-canted structure of $EuCd_2As_2$ *Phys. Rev.* B **105** L140401

[16] Cao X *et al* 2022 Giant nonlinear anomalous Hall effect induced by spin-dependent band structure evolution *Phys. Rev. Res.* **4** 023100

[17] Xu Y *et al* 2021 Unconventional transverse transport above and below the magnetic transition temperature in Weyl semimetal $EuCd_2As_2$ *Phys. Rev. Lett.* **126** 076602

[18] Wu W B *et al* 2024 The discovery of three-dimensional van Hove singularity *Nat. Commun.* **15** 2313

[19] Wang Y *et al* 2022 Giant and reversible electronic structure evolution in a magnetic topological material $EuCd_2As_2$ *Phys. Rev.* B **106** 085134

[20] Sun Y *et al* 2022 Experimental evidence for field-induced metamagnetic transition of $EuCd_2As_2$ *J. Rare Earth* **40** 1606–10

[21] Du Y, Chen J, Wu W, Shi Z, Meng X, Zhang C, Gong S, Chu J and Yuan X 2022 Comparative Raman spectroscopy of magnetic topological material $EuCd_2X_2$ (X=P, As) *J. Phys.: Condens. Matter* **34** 224001

[22] Jo N H *et al* 2021 Visualizing band selective enhancement of quasiparticle lifetime in a metallic ferromagnet *Nat. Commun.* **12** 7169

[23] Niu C, Mao N, Hu X, Huang B and Dai Y 2019 Quantum anomalous Hall effect and gate-controllable topological phase transition in layered $EuCd_2As_2$ *Phys. Rev.* B **99** 235119

[24] Krishna J, Nautiyal T and Maitra T 2018 First-principles study of electronic structure, transport, and optical properties of $EuCd_2As_2$ *Phys. Rev.* B **98** 125110

[25] Santos-Cottin D *et al* 2023 2023 $EuCd_2As_2$: a magnetic semiconductor *Phys. Rev. Lett.* **131** 186704

[26] Shi Y *et al* 2024 Absence of Weyl nodes in $EuCd_2As_2$ revealed by the carrier density dependence of the anomalous Hall effect *Phys. Rev.* B **109** 125202

[27] Wang Y *et al* 2024 Absence of metallicity and bias-dependent resistivity in low-carrier-density $EuCd_2As_2$ *Sci. China Phys. Mech.* **67** 247311

[28] Cuono G, Sattigeri R M, Autieri C and Dietl T 2023 *Ab initio* overestimation of the topological region in Eu-based compounds *Phys. Rev.* B **108** 075150

[29] Wang Z-C *et al* 2022 Anisotropy of the magnetic and transport properties of $EuZn_2As_2$ *Phys. Rev.* B **105** 165122

[30] Blawat J, Marshall M, Singleton J, Feng E, Cao H, Xie W and Jin R 2022 Unusual electrical and magnetic properties in layered $EuZn_2As_2$ *Adv. Quantum Technol.* **5** 2200012

[31] Luo S, Xu Y, Du F, Yang L, Chen Y, Cao C, Song Y and Yuan H 2023 Colossal magnetoresistance and topological phase transition in $EuZn_2As_2$ *Phys. Rev.* B **108** 205140

[32] Berry T, Stewart V J, Redemann B W Y, Lygouras C, Varnava N, Vanderbilt D and McQueen T M 2022 A-type antiferromagnetic order in the Zintl-phase insulator $EuZn_2P_2$ *Phys. Rev.* B **106** 054420

[33] Krebber S *et al* 2023 Colossal magnetoresistance in $EuZn_2P_2$ and its electronic and magnetic structure *Phys. Rev.* B **108** 045116

[34] Wang Z-C *et al* 2021 Colossal magnetoresistance without mixed valence in a layered phosphide crystal *Adv. Mater.* **33** 2005755

[35] Zhang H *et al* 2023 Electronic band reconstruction across the insulator-metal transition in colossally magnetoresistive $EuCd_2P_2$ *Phys. Rev.* B **108** L241115

[36] Jo N H *et al* 2020 Manipulating magnetism in the topological semimetal $EuCd_2As_2$ *Phys. Rev.* B **101** 140402(R)

[37] Roychowdhury S *et al* 2023 Anomalous Hall conductivity and Nernst effect of the ideal Weyl semimetallic ferromagnet $EuCd_2As_2$ *Adv. Sci.* **10** 2207121

[38] Chen X, Yang W, Lu J-Y, Zhou Z, Ren Z, Cao G-H, Dong S and Wang Z-C 2024 Carrier-induced transition from antiferromagnetic insulator to ferromagnetic metal in the layered phosphide $EuZn_2P_2$ *Phys. Rev.* B **109** L180410

[39] Chen X *et al* 2024 Manipulating magnetism and transport properties of $EuCd_2P_2$ with a low carrier concentration *Phys. Rev.* B **109** 224428

[40] Jimenez J L G *et al* 2023 Tetragonal kondo insulator $EuCd_2Sb_2$ discovered via high pressure high temperature synthesis *Adv. Funct. Mater.* **33** 2303612

[41] Su H *et al* 2020 Magnetic exchange induced Weyl state in a semimetal $EuCd_2Sb_2$ *APL Mater.* **8** 011109

[42] Singh K, Pavlosiuk O, Dan S, Kaczorowski D and Wiśniewski P 2024 Large unconventional anomalous Hall effect arising from spin chirality within domain walls of an antiferromagnet $EuZn_2Sb_2$ *Phys. Rev.* B **109** 125107

[43] Villars P and Cenzual K 2013 *Handbook of Inorganic Substances 2013* (Walter de Gruyter)

[44] Pakhira S *et al* 2023 Anisotropic magnetism and electronic structure of trigonal $EuAl_2Ge_2$ single crystals *Phys. Rev.* B **107** 134439

[45] Pakhira S, Heitmann T, Riberolles S X M, Ueland B G, McQueeney R J, Johnston D C and Vaknin D 2021 Zero-field magnetic ground state of $EuMg_2Bi_2$ *Phys. Rev.* B **103** 024408

[46] Anand V K and Johnston D C 2016 Metallic behavior induced by potassium doping of the trigonal antiferromagnetic insulator $EuMn_2As_2$ *Phys. Rev.* B **94** 014431

[47] Pomrehn G S, Zevalkink A, Zeier W G, van de Walle A and Snyder G J 2014 Defect-controlled electronic properties in AZn_2Sb_2 Zintl phases *Angew. Chem., Int. Ed. Engl.* **53** 3422

[48] Toberer E S, May A F, Melot B C, Flage-Larsen E and Snyder G J 2010 Electronic structure and transport in thermoelectric compounds AZn_2Sb_2 (A = Sr, Ca, Yb, Eu) *Dalton Trans.* **39** 1046

[49] Peng W, Chanakian S and Zevalkink A 2018 Crystal chemistry and thermoelectric transport of layered AM_2X_2 compounds *Inorg. Chem. Front.* **5** 1744

[50] Chen X, Wang S, Wang J, An C, Zhou Y, Chen Z, Zhu X, Zhou Y, Yang Z and Tian M 2023 Temperature-pressure phase diagram of the intrinsically insulating topological antiferromagnet $EuCd_2As_2$ *Phys. Rev.* B **107** L241106

[51] Usachov D Y *et al* 2024 Magnetism, heat capacity, and electronic structure of $EuCd_2P_2$ in view of its colossal magnetoresistance *Phys. Rev.* B **109** 104421

[52] Singh K, Dan S, Ptok A, Zaleski T A, Pavlosiuk O, Wiśniewski P and Kaczorowski D 2023 Superexchange interaction in insulating $EuZn_2P_2$ *Phys. Rev.* B **108** 054402

[53] Soh J R, Schierle E, Yan D Y, Su H, Prabhakaran D, Weschke E, Guo Y F, Shi Y G and Boothroyd A T 2020 Resonant x-ray scattering study of diffuse magnetic scattering from the topological semimetals $EuCd_2As_2$ and $EuCd_2Sb_2$ *Phys. Rev.* B **102** 014408

[54] Sunko V *et al* 2023 Spin-carrier coupling induced ferromagnetism and giant resistivity peak in $EuCd_2P_2$ *Phys. Rev.* B **107** 144404

[55] Yi E *et al* 2023 Topological Hall effect driven by short-range magnetic order in $EuZn_2As_2$ *Phys. Rev.* B **107** 035142

[56] Lv B Q, Qian T and Ding H 2021 Experimental perspective on three-dimensional topological semimetals *Rev. Mod. Phys.* **93** 025002

[57] Heinrich E, Posske T and Flebus B 2022 Topological magnetic phase transition in Eu-based A-type antiferromagnets *Phys. Rev.* B **106** 214402

[58] Flebus B 2021 Magnetoresistance driven by the magnetic Berezinskii-Kosterlitz-Thouless transition *Phys. Rev.* B **104** L020408

[59] Homes C C, Wang Z C, Fruhling K and Tafti F 2023 Optical properties and carrier localization in the layered phosphide $EuCd_2P_2$ *Phys. Rev.* B **107** 045106

[60] Blawat J, Speer S, Singleton J, Xie W and Jin R 2023 Quantum-limit phenomena and band structure in the magnetic topological semimetal $EuZn_2As_2$ *Commun. Phys.* **6** 255

[61] Gati E *et al* 2021 Pressure-induced ferromagnetism in the topological semimetal $EuCd_2As_2$ *Phys. Rev.* B **104** 155124

[62] Pari N A Á, Bharadwaj V K, Jaeschke-Ubiergo R, Valadkhani A, Valentí R, Šmejkal L and Sinova J 2024 Strain control of band topology and surface states in antiferromagnetic $EuCd_2As_2$ *Phys. Rev.* B **109** 195117

[63] Yu Z *et al* 2023 Structure, magnetotransport, and theoretical study on the layered antiferromagnet topological phase $EuCd_2As_2$ under high pressure *Adv. Quantum Technol.* **6** 2200128

[64] Valadkhani A, Iraola M, Fünfhaus A, Song Y-J, Šmejkal L, Sinova J and Valentí R 2023 Influence of magnetism, strain, and pressure on the band topology of $EuCd_2As_2$ *Phys. Rev.* B **108** 235113

[65] Jose G C *et al* 2023 Evolution of magnetism, valence, and crystal lattice in $EuCd_2As_2$ under pressure *Phys. Rev.* B **107** 245121

[66] Du F *et al* 2022 Consecutive topological phase transitions and colossal magnetoresistance in a magnetic topological semimetal *npj Quantum Mater.* **7** 65

[67] Rybicki D *et al* 2024 Ambient- and high-pressure studies of structural, electronic, and magnetic properties of single-crystal $EuZn_2P_2$ *Phys. Rev.* B **110** 014421

[68] Kuthanazhi B, Joshi K R, Ghimire S, Timmons E, Wang L-L, Gati E, Xiang L, Prozorov R, Bud'ko S L and Canfield P C 2023 Magnetism and $T-x$ phase diagrams of Na- and Ag-substituted $EuCd_2As_2$ *Phys. Rev. Mater.* **7** 034402

[69] Nelson R A *et al* 2024 Revealing the $EuCd_2As_2$ semiconducting band gap via n-type La-doping *Chem. Mater.* **36** 7623

[70] Sanjeewa L D, Xing J, Taddei K M, Parker D, Custelcean R, Dela Cruz C and Sefat A S 2020 Evidence of Ba-substitution induced spin-canting in the magnetic Weyl semimetal $EuCd_2As_2$ *Phys. Rev.* B **102** 104404

[71] Mauger A 1977 Indirect exchange in europium chalcogenides *Phys. Stat. Solidi* **84** 761

[72] Mauger A and Godart C 1986 The magnetic, optical, and transport properties of representatives of a class of magnetic semiconductors: the europium chalcogenides *Phys. Rep.* **141** 51

[73] Ohno H 1998 Making nonmagnetic semiconductors ferromagnetic *Science* **281** 951

[74] Matsukura F, Ohno H, Shen A and Sugawara Y 1998 Transport properties and origin of ferromagnetism in (Ga,Mn)As *Phys. Rev.* B **57** R2037

[75] Majumdar P and Littlewood P 1998 Magnetoresistance in Mn pyrochlore: electrical transport in a low carrier density ferromagnet *Phys. Rev. Lett.* **81** 1314

[76] Young D P, Hall D, Torelli M E, Fisk Z, Sarrao J L, Thompson J D, Ott H-R, Oseroff S B, Goodrich R G and Zysler R 1999 High-temperature weak ferromagnetism in a low-density free-electron gas *Nature* **397** 412

[77] Süllow S, Prasad I, Bogdanovich S, Aronson M C, Sarrao J L and Fisk Z 2000 Magnetotransport in the low carrier density ferromagnet EuB_6 *J. Appl. Phys.* **87** 5591

[78] Tateiwa N, Haga Y, Sakai H and Yamamoto E 2019 Novel universality class for the ferromagnetic transition in the low carrier concentration systems UTeS and USeS exhibiting large negative magnetoresistance *Phys. Rev.* B **100** 064413

[79] Story T, Gałązka R R, Frankel R B and Wolff P A 1986 Carrier-concentration–induced ferromagnetism in PbSnMnTe *Phys. Rev. Lett.* **56** 777

[80] Miyazaki H, Im H J, Terashima K, Yagi S, Kato M, Soda K, Ito T and Kimura S 2010 La-doped EuO: a rare earth ferromagnetic semiconductor with the highest Curie temperature *Appl. Phys. Lett.* **96** 232503

[81] Schmehl A *et al* 2007 Epitaxial integration of the highly spin-polarized ferromagnetic semiconductor EuO with silicon and GaN *Nat. Mater.* **6** 882

[82] Von Molnar S and Methfessel S 1967 Giant negative magnetoresistance in ferromagnetic $Eu_{1-x}Gd_xSe$ *J. Appl. Phys.* **38** 959

[83] Majumdar P and Littlewood P B 1998 Dependence of magnetoresistivity on charge-carrier density in metallic ferromagnets and doped magnetic semiconductors *Nature* **395** 479

[84] Ohno M, Minami S, Nakazawa Y, Sato S, Kriener M, Arita R, Kawasaki M and Uchida M 2022 Maximizing intrinsic anomalous Hall effect by controlling the Fermi level in simple Weyl semimetal films *Phys. Rev.* B **105** L201101

[85] Nishihaya S, Nakamura A, Ohno M, Kriener M, Watanabe Y, Kawasaki M and Uchida M 2024 Intrinsic insulating transport characteristics in low-carrier density $EuCd_2As_2$ films *Appl. Phys. Lett.* **124** 023103

[86] Nakamura A, Nishihaya S, Ishizuka H, Kriener M, Ohno M, Watanabe Y, Kawasaki M and Uchida M 2024 Berry curvature derived negative magnetoconductivity observed in type-II magnetic Weyl semimetal films *Phys. Rev.* B **109** L121108

[87] Matsuoka H, Fujishiro Y, Minami S, Koretsune T, Arita R, Tokura Y and Iwasa Y Electron-doped magnetic Weyl semimetal $Li_xCo_3Sn_2S_2$ by bulk-gating (arXiv:2312.17547)

[88] Pakhira S, Islam F, O'Leary E, Tanatar M A, Heitmann T, Wang -L-L, Prozorov R, Kaminski A, Vaknin D and Johnston D C 2022 A-type antiferromagnetic order in semiconducting $EuMg_2Sb_2$ single crystals *Phys. Rev.* B **106** 024418

[89] Weber F, Cosceev A, Drobnik S, Faißt A, Grube K, Nateprov A, Pfleiderer C, Uhlarz M and Löhneysen H V 2006 Low-temperature properties and magnetic order of $EuZn_2Sb_2$ *Phys. Rev.* B **73** 014427

[90] Soh J R, Donnerer C, Hughes K M, Schierle E, Weschke E, Prabhakaran D and Boothroyd A T 2018 Magnetic and electronic structure of the layered rare-earth pnictide $EuCd_2Sb_2$ *Phys. Rev.* B **98** 064419

[91] Berry T *et al* 2023 Bonding and suppression of a magnetic phase transition in $EuMn_2P_2$ *J. Am. Chem. Soc.* **145** 4527